nature medicine

LETTERS

Human induced pluripotent stem cell–derived cardiomyocytes recapitulate the predilection of breast cancer patients to doxorubicin-induced cardiotoxicity

Paul W Burridge[1–5], Yong Fuga Li[6,7], Elena Matsa[1–3], Haodi Wu[1–3], Sang-Ging Ong[1–3], Arun Sharma[1–3], Alexandra Holmström[1–3], Alex C Chang[1,2,8], Michael J Coronado[9], Antje D Ebert[1–3], Joshua W Knowles[1,3], Melinda L Telli[10], Ronald M Witteles[1,3], Helen M Blau[1,2,8], Daniel Bernstein[1,9], Russ B Altman[7,11] & Joseph C Wu[1–3]

© 2016 Nature America, Inc. All rights reserved.

Doxorubicin is an anthracycline chemotherapy agent effective in treating a wide range of malignancies, but it causes a dose-related cardiotoxicity that can lead to heart failure in a subset of patients. At present, it is not possible to predict which patients will be affected by doxorubicin-induced cardiotoxicity (DIC). Here we demonstrate that patient-specific human induced pluripotent stem cell–derived cardiomyocytes (hiPSC-CMs) can recapitulate the predilection to DIC of individual patients at the cellular level. hiPSC-CMs derived from individuals with breast cancer who experienced DIC were consistently more sensitive to doxorubicin toxicity than hiPSC-CMs from patients who did not experience DIC, with decreased cell viability, impaired mitochondrial and metabolic function, impaired calcium handling, decreased antioxidant pathway activity, and increased reactive oxygen species production. Taken together, our data indicate that hiPSC-CMs are a suitable platform to identify and characterize the genetic basis and molecular mechanisms of DIC.

The anthracycline doxorubicin (trade name Adriamycin) was first introduced in the 1960s and remains one of the most effective and commonly used antineoplastic drugs[1]. Despite the advent of targeted tyrosine kinase– and monoclonal-antibody-based therapies, anthracyclines are still prescribed to 40–50% of individuals with breast cancer[2], typically alongside the alkylating agent cyclophosphamide (trade name Cytoxan), or the antimicrotubule taxanes paclitaxel (trade name Taxol) or docetaxel (trade name Taxotere). The dose-dependent cardiotoxicity of doxorubicin is well established[3,4]. Even at relatively low cumulative doses of 200–250 mg m^{-2}, the risk of cardiotoxicity is estimated at 7.8% to 8.8% (refs. 5,6). Cardiotoxic side effects experienced with doxorubicin treatment range from asymptomatic increases in left ventricular wall stress to reductions in left ventricular ejection fraction (LVEF), arrhythmias, and highly symptomatic congestive heart failure, which are often severe enough to warrant heart transplantation[7–9]. At present, it is not possible to predict which patients will be affected by DIC or to adequately protect patients who are at risk for suffering from this devastating side effect[10].

Three major mechanisms have been proposed for the anticancer effects of doxorubicin: stabilization of the topoisomerase II-α (TOP2A)–DNA cleavage complex and prevention of DNA religation and double-stranded break repair; intercalation with double-stranded DNA directly, leading to transcriptomic and epigenetic modulation, and inhibition of DNA replication; and generation of free radicals that cause damage to DNA, cellular proteins, and mitochondria.

The mechanisms that account for the cardiotoxic effects of doxorubicin are believed to be more complex but can be grouped into three interrelated subsets: generation of reactive oxygen species (ROS) and subsequent membrane damage[11]; inhibition of topoisomerase II-β (TOP2B)[12] and topoisomerase I mitochondrial (TOP1MT)[13]; and modulation of intracellular calcium release[14]. Generation of ROS by redox cycling between the quinone and semiquinone forms of doxorubicin within cardiomyocytes, which is both dependent on and independent of iron, causes mitochondrial dysregulation, lipid peroxidation, DNA damage, and protein carbonylation. ROS can be deactivated by endogenous antioxidants such as glutathione peroxidase, catalase, and superoxide dismutase, but doxorubicin also directly reduces the activity of these antioxidants, further increasing

[1]Stanford Cardiovascular Institute, Stanford University School of Medicine, Stanford, California, USA. [2]Institute for Stem Cell Biology and Regenerative Medicine, Stanford University School of Medicine, Stanford, California, USA. [3]Department of Medicine, Division of Cardiovascular Medicine, Stanford University School of Medicine, Stanford, California, USA. [4]Department of Pharmacology, Northwestern University Feinberg School of Medicine, Chicago, Illinois, USA. [5]Center for Pharmacogenomics, Northwestern University Feinberg School of Medicine, Chicago, Illinois, USA. [6]Stanford Genome Technology Center, Stanford University School of Medicine, Stanford, California, USA. [7]Department of Bioengineering, Stanford University School of Medicine, Stanford, California, USA. [8]Department of Microbiology and Immunology, Stanford University School of Medicine, Stanford, California, USA. [9]Department of Pediatrics, Division of Cardiology, Stanford University School of Medicine, Stanford, California, USA. [10]Department of Medicine, Division of Oncology, Stanford University School of Medicine, Stanford, California, USA. [11]Department of Genetics, Stanford University School of Medicine, Stanford, California, USA. Correspondence should be addressed to P.W.B. (paul.burridge@northwestern.edu) or J.C.W. (joewu@stanford.edu).

Received 14 December 2015; accepted 18 March 2016; published online 18 April 2016; doi:10.1038/nm.4087

oxidative stress[7]. Mitochondria are the major site of doxorubicin-induced ROS generation because the major redox cycling compounds, such as NAD(P)H, are localized to this organelle and because doxorubicin binds irreversibly to cardiolipin, a component of the inner mitochondrial membrane, thereby concentrating the drug in this location[15]. Doxorubicin also increases mitochondrial iron accumulation, further increasing ROS production in the mitochondria[16]. Topoisomerase inhibition (including inhibition of both TOP2B and TOP1MT) causes transcriptional modulation of nuclear and mitochondrial genes and DNA-damage-induced apoptosis. Specifically, TOP2B has been associated with a reduction in mitochondrial biogenesis that is mediated by peroxisome proliferator-activated receptor gamma (PPARG) coactivator 1-α and (PPARGC1A) and PPARG coactivator 1-β (PPARGC1B)[12]. Finally, doxorubicin and its metabolite doxorubicinol can induce Ca^{2+} release from the sarcoplasmic reticulum, causing Ca^{2+} overload that leads to sarcomeric disarray and myofibril deterioration[14,17].

Here we demonstrate the ability of hiPSC-CMs derived from individuals with breast cancer who experienced DIC in recapitulating this phenotype *in vitro*, validating hiPSC-CMs as a platform for predicting DIC severity in patients and for identifying the pharmacogenomic mechanisms of DIC. As the molecular effects of doxorubicin on human hearts are essentially unknown, we extensively probed the transcriptomes of hiPSC-CMs derived from multiple doxorubicin-treated patients. Notably, we found that hiPSC-CMs from individuals who experienced cardiotoxicity, as compared to those from individuals who did not, showed substantially lower levels of basal metabolism and mitochondrial content, which may be key factors contributing to DIC.

RESULTS

Generation of patient-specific hiPSC-derived cardiomyocytes

We recruited 12 female patients—eight with breast cancer who had been treated at Stanford University Hospital with 240 mg m^{-2} doxorubicin or the equivalent (**Supplementary Tables 1** and **2**), including four patients (referred to as 'DOX') who did not experience clinical cardiotoxicity (as documented by a post-treatment LVEF > 55%) and four patients ('DOXTOX') who did experience clinical cardiotoxicity (post-treatment LVEF = 10–45%)—and four age- and gender-matched control volunteers who had never been treated with any chemotherapeutic agent ('healthy') (**Supplementary Table 2**). We derived hiPSCs from the skin fibroblasts of these individuals[18], and all cell lines passed standard tests for pluripotency[19] and genomic stability[20] (**Supplementary Figs. 1** and **2**). Next we differentiated the patient-derived hiPSCs into cardiomyocytes[21], with modifications to the cell differentiation protocol to enhance cardiomyocyte purity[22], mitochondrial metabolism[23], and maturation[24], resulting in cell preparations of >85% cardiomyocytes (**Supplementary Fig. 3**). We based the dose of doxorubicin for the *in vitro* treatment of hiPSC-CMs on the pharmacokinetic characteristics of doxorubicin in humans—the terminal plasma half-life of doxorubicin is 20–48 h, and the peak plasma concentration (C_{max}) is 2–6 μg ml^{-1} (the average value is 6.9 μM) for a single dose of 60 mg m^{-2} (refs. 25,26). Therefore, we primarily used doxorubicin at concentrations in this range (0.1–10.0 μM). We selected time points of 24 h and 72 h for cell treatment on the basis of prior reports in which primary neonatal rat ventricular cardiomyocytes (NRVMs) were treated with doxorubicin[27–29].

Characterization of *in vitro* doxorubicin-induced cardiotoxicity

We first tested whether a differential response to doxorubicin exists among the healthy, DOX, and DOXTOX hiPSC-CM groups. A concentration-dependent increase in sarcomeric disarray is a well-established effect of doxorubicin on NRVMs[30,31]. As assessed by immunofluorescent imaging, we observed a consistent effect of sarcomeric disarray in DOXTOX but not DOX cells that were treated with 0.1 μM doxorubicin (**Fig. 1a**). Cardiomyocyte contraction assays demonstrated that treatment with 1 μM doxorubicin resulted in increased rates of beating in both DOX and DOTOX cells, as compared to those at the 0 μM doxorubicin baseline; doxorubicin at higher concentrations led to arrhythmic beating, which was more severe in DOXTOX than in DOX cells (**Fig. 1b**,**c**). After a 72-h treatment with doxorubicin, the four DOXTOX hiPSC-CM lines consistently showed significantly reduced cell viability as compared to the four DOX and the four healthy hiPSC-CM lines at all concentrations tested (F–test statistic = 170.5, $P < 0.0001$), with half-maximal lethal doses (LD_{50}) of 0.1643 μM and 3.015 μM for DOXTOX and DOX cells, respectively (**Fig. 1d**). This increase in doxorubicin cardiotoxicity susceptibility was further validated using a wide range of parameters, including membrane integrity and maintenance of a reducing environment, ATP concentration, adenylate kinase release, and lactate dehydrogenase release (**Supplementary Fig. 4a**–**e**). Flow cytometry analysis demonstrated a concentration-dependent increase in cells that stained positive for both annexin V and 7-aminoactinomycin D (7-AAD) (**Fig. 1e**), suggesting that programmed cell death was the principal mechanism of cell loss. Moreover, at high doxorubicin concentrations, DOXTOX hiPSC-CMs had significantly ($P < 0.005$) higher percentages of annexin $V^+7\text{-}AAD^+$ cells than DOX hiPSC-CMs (**Fig. 1e**). Measurement of active caspase 3 and caspase 7 levels confirmed this result (**Fig. 1f**).

Given that the major therapeutic mechanism for doxorubicin in tumor cells is induction of DNA damage, we next assessed the level of double-stranded DNA damage by staining for phosphorylated H2A histone family member X (γ-H2AX). We observed a concentration-dependent increase in DNA damage (**Fig. 2a**), and the level of DNA damage was significantly ($P < 0.005$) higher in DOXTOX hiPSC-CMs than in DOX hiPSC-CMs at doxorubicin concentrations of 0.1 μM and 1 μM (**Fig. 2b**). To probe potential mechanisms for the observed differences in response to doxorubicin, we assessed spontaneous Ca^{2+} transients by loading single cells with the Ca^{2+} indicator dye Fluo-4 (**Fig. 2c**). At concentrations of 1 μM or 10 μM doxorubicin, DOXTOX hiPSC-CMs had a significantly higher ($P < 0.005$) transient decay time (decay τ) as compared to DOXTOX hiPSC-CMs (**Fig. 2d**); this difference is probably a function of the reduced Ca^{2+}-transient amplitude and time-to-peak Ca^{2+} signal in the DOXTOX hiPSC-CMs, as compared to those in the DOX and healthy hiPSC-CMs (**Supplementary Fig. 4f**,**g**). No significant differences in beat rate between groups were detected (**Supplementary Fig. 4h**).

Several studies have implicated oxidative stress as the central mechanism underlying the cardiotoxic effects of doxorubicin[32–35]. We next assessed cellular ROS production by flow cytometry using the fluorescent CellROX probe. After 24 h of doxorubicin treatment, ROS levels were significantly ($P < 0.005$) higher in DOXTOX hiPSC-CMs than in DOX hiPSC-CMs, by an average of >2-fold over a concentration range of 0.1–10.0 μM (**Fig. 2e**). A second assay measuring whole-cell hydrogen peroxide (H_2O_2) levels confirmed this >2-fold increase in ROS levels at concentrations of doxorubicin as low as 0.01 μM (**Fig. 3a**). We also measured levels of the antioxidant glutathione (GSH) as a marker of cellular oxidative stress response in doxorubicin-treated cells. As compared to DOX hiPSC-CMs, DOXTOX hiPSC-CMs showed a significant ($P < 0.005$) reduction in GSH levels at all but the lowest concentrations of doxorubicin (half-maximal effective

© 2016 Nature America, Inc. All rights reserved.

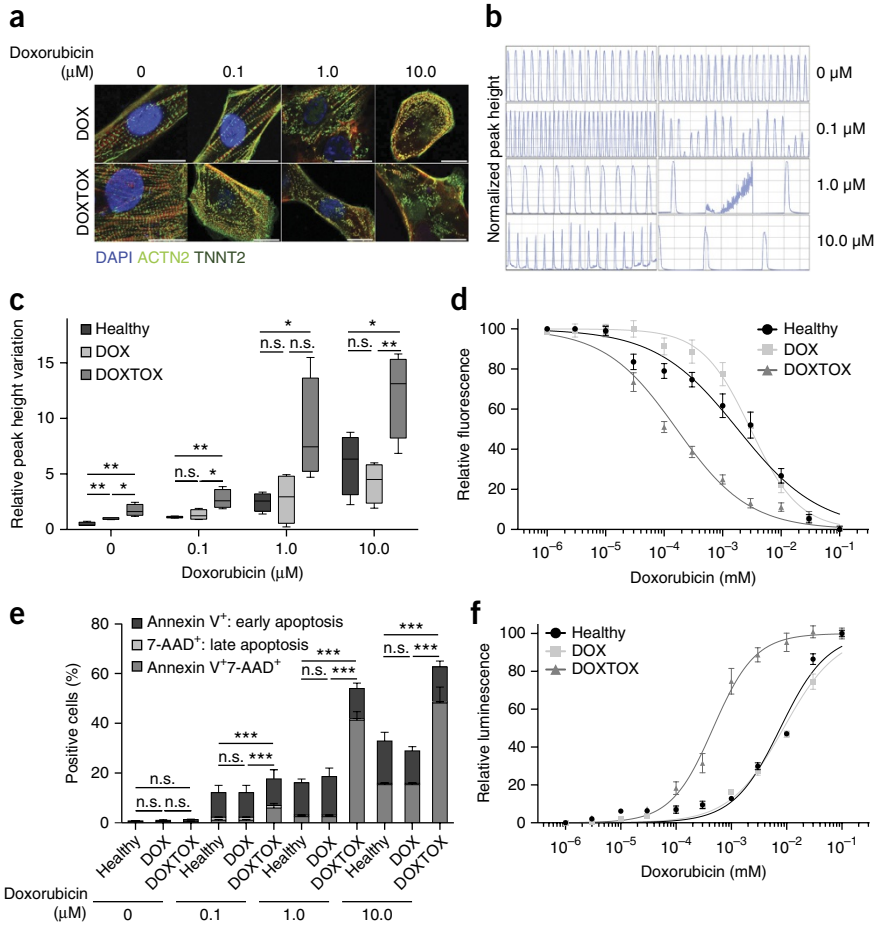

Figure 1 Assessment of *in vitro* doxorubicin-induced cardiotoxicity in patient-specific hiPSC-CMs. (**a**) Representative images for sarcomeric organization in hiPSC-CMs derived from individuals who did not experience doxorubicin-induced cardiotoxicity (DOX; $n = 8$) (top) versus those who did (DOXTOX; $n = 8$) (bottom), after 24 h treatment with doxorubicin at the indicated concentrations, as assessed by immunofluorescence staining for α-actinin (ACTN2) and cardiac troponin T (TNNT2). Scale bars, 10 μm. (**b**) Representative camera-capture contraction assays demonstrating variation in beat frequency of DOX1 (left) and DOXTOX4 (right) hiPSC-CMs in response to treatment with the indicated concentrations of doxorubicin for 24 h (DOX, $n = 4$; DOXTOX, $n = 4$). (**c**) Quantification of relative peak height from the camera-capture contraction assay, after treatment of healthy, DOX, and DOXTOX hiPSC-CMs with the indicated concentrations of doxorubicin for 24 h. The data were obtained using hiPSC-CMs from four patients per group, one cell line per patient, and the assay was repeated three times ($n = 12$). (**d**) Effect of doxorubicin (72 h) on hiPSC-CM viability ($n = 12$ per group) using a PrestoBlue resazurin–based dye assay. LD_{50}: healthy, 1.8200 μM; DOX, 3.015 μM; DOXTOX, 0.1643 μM. (**e**) Effect of doxorubicin on early (annexin V^+ cells) and late (7-AAD^+ cells) apoptosis of hiPSC-CMs after 72 h treatment with doxorubicin. The data were obtained using hiPSC-CMs from four patients per group, one cell line per patient ($n = 4$). (**f**) Effect of doxorubicin (72 h) on caspase 3 and caspase 7 activity, as assessed by using a luminescent Caspase-Glo assay. The data were obtained using hiPSC-CMs from four patients per group, one cell line per patient, and the assay was repeated twice ($n = 8$). Throughout, data are represented as mean ± s.e.m. $^*P < 0.05$; $^{**}P < 0.01$; $^{***}P < 0.005$; n.s., not significant; by unpaired two-tailed Student's *t*-test.

concentration (EC_{50}) of 0.04 μM for DOXTOX hiPSC-CMs versus 0.8 μM for DOX hiPSC-CMs) (**Fig. 3b**). Mitochondria are one of the major sources of ROS production and also a target for doxorubicin toxicity. Using a mitochondrial superoxide probe (MitoSOX), which detects mitochondrial superoxides but not other types of reactive oxygen or nitrogen species, we demonstrated that there were significantly ($P < 0.005$) higher levels of mitochondrial ROS in DOXTOX hiPSC-CMs than in DOX hiPSC-CMs (>2.5-fold at 10 μM) (**Fig. 3c**). Finally, using the JC-10 mitochondrial membrane potential ($\Delta\Psi_m$) probe, we demonstrated a dose-dependent decrease in $\Delta\Psi_m$ for doxorubicin. In the concentration range of 0.1 to 10 μM doxorubicin, this decrease was significantly ($P < 0.01$) greater in DOXTOX hiPSC-CMs than in DOX hiPSC-CMs (**Fig. 3d**).

To further study the mechanism of action of doxorubicin, we next treated hiPSC-CMs with the cardioprotectant dexrazoxane (DRZ)[36], a topoisomerase 2 inhibitor and iron chelator that is used clinically to reduce DIC[37], both before and concurrently with doxorubicin treatment. Unexpectedly, we found that DRZ treatment significantly ($P < 0.005$) increased doxorubicin-induced toxicity, specifically in DOXTOX hiPSC-CMs treated with 0.1 μM doxorubicin and in DOX hiPSC-CMs treated with 3 μM doxorubicin (**Fig. 3e**). To determine whether this effect was a general one in this model or limited to this one agent, we assessed the effects of a well-established antioxidant, *N*-acetyl-L-cysteine (NAC)[38]. NAC treatment significantly ($P < 0.005$) decreased DIC in DOXTOX hiPSC-CMs (**Fig. 3f**), confirming that ROS-based toxicity is a major component of the reduced viability of doxorubicin-treated cells.

Effects of doxorubicin on patient-specific gene expression

We hypothesized that the mechanisms underlying DIC may vary depending on the concentration of doxorubicin used. To probe this issue, we performed microarray analysis on human embryonic stem cell (hESC)-derived cardiomyocytes (hESC-CMs) exposed to increasing concentrations of doxorubicin (**Fig. 4a**). After a 24-h doxorubicin treatment, minimal changes were seen at a concentration of 0.1 μM. In contrast, at a concentration of 1 μM, the expression of genes encoding numerous cardiac-development-related transcription factors was significantly downregulated, as compared to the untreated group, including the expression of genes encoding NK2 homeobox 5 (*NKX2-5*), myocyte enhancer factor 2A (*MEF2A*), T-box 5 (*TBX5*), and myocardin (*MYOCD*) (**Supplementary Table 3**). Using Ingenuity Toxicogenomics analysis, we found that the categories of transforming growth factor (TGF)-β signaling, the tumor suppressor p53, cardiac hypertrophy, G1/S cell cycle checkpoint regulation, and retinoic acid receptor (RAR) activation were differentially regulated between the groups treated with 1 μM and 10 μM doxorubicin (**Supplementary Table 4**). We next applied an unsupervised machine-learning approach, independent component analysis[39], and identified eight modules of gene expression that correlated with the different concentrations of doxorubicin (**Fig. 4a**). The genes

© 2016 Nature America, Inc. All rights reserved.

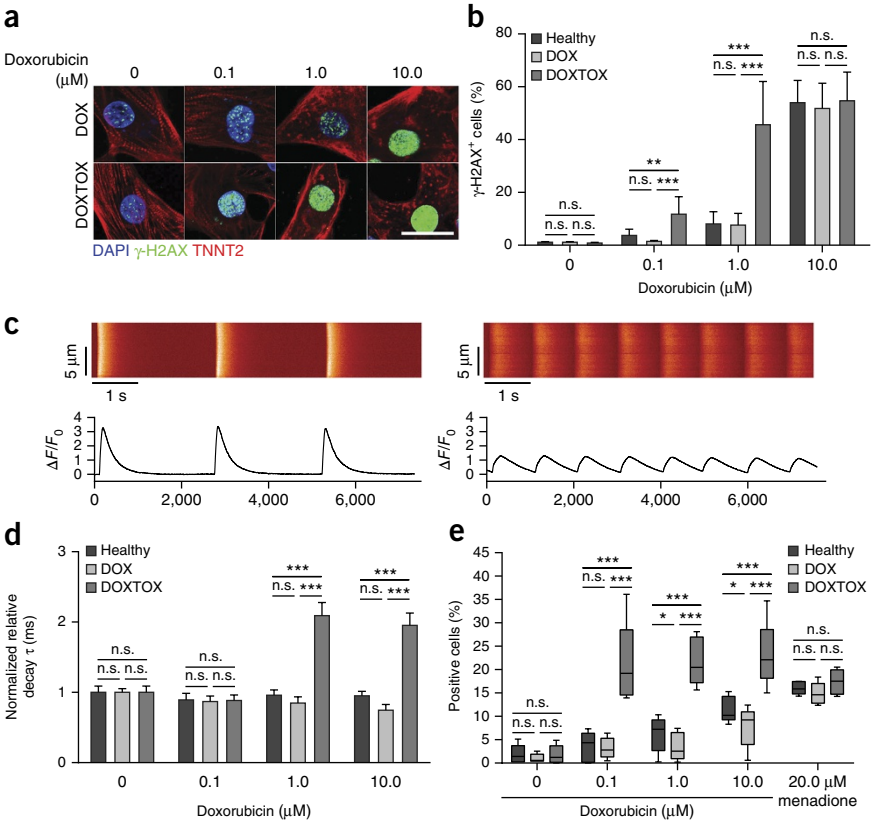

Figure 2 Assessment of the effects of doxorubicin on DNA damage, calcium handling, and whole-cell oxidative stress in patient-specific hiPSC-CMs. (**a**) Representative images for detection of DNA double-stranded breaks, as assessed by immunofluorescent staining for γ-H2AX, after treatment of DOX ($n = 4$) (top) or DOXTOX ($n = 4$) (bottom) hiPSC-CMs with the indicated concentrations of doxorubicin for 24 h. Scale bar, 20 μm. (**b**) Quantification of γ-H2AX staining by flow cytometry. The data were obtained using hiPSC-CMs from four patients per group, one cell line per patient ($n = 4$ per group). (**c**) Representative recording of spontaneous calcium activity of patient-derived hiPSC-CMs at baseline (left) or after treatment with doxorubicin (right). Data for the DOXTOX1 cell line is shown. $\Delta F/F_0$, change in fluorescence intensity in relationship to resting fluorescence intensity. (**d**) Normalized relative decay τ, as measured by calcium imaging. The data were obtained using four hiPSC-CM lines per group ($n > 35$ cells per line). Values were normalized to that of the 0 μM healthy group. (**e**) Effects of doxorubicin treatment for 24 h (before cell death) on whole-cell ROS levels using a dye which stains for whole-cell ROS (CellROX). Treatment with menadione, a synthetic naphthoquinone that induces the formation of ROS, was used as a positive control.The data were obtained using hiPSC-CMs from four patients per group, one cell line per patient ($n = 4$). Throughout, data are represented as mean ± s.e.m. $^*P < 0.05$, $^{**}P < 0.01$, $^{***}P < 0.005$, n.s., not significant; by Fisher's exact test, one-way analysis of variance (ANOVA) test followed by all-pairwise-multiple-comparison procedures (Holm–Sidak method) (**d**) or by unpaired two-tailed Student's *t*-test (**b**,**e**).

incorporated into these modules included key transcription regulators—such as *TP53* (which encodes p53), *RELA* (which encodes v-rel avian reticuloendotheliosis viral oncogene homolog A), *NFKB1* (which encodes nuclear factor of kappa light polypeptide gene enhancer in B cells 1), and *EP300* (which encodes E1A-binding protein p300)—that have previously been implicated in doxorubicin pharmacodynamics and cardiotoxicity pathways by an analysis using PharmGKB, an established comprehensive database of gene and drug response interactions[40] (**Fig. 4b** and **Supplementary Fig. 5a**,**b**).

To identify a transcriptomic basis for the observed differences in response to doxorubicin in the DOX and DOXTOX cell groups, we performed RNA-seq analysis on hiPSC-CMs derived from three DOX and three DOXTOX lines, both with and without 1 μM doxorubicin treatment for 24 h. After normalizing for baseline expression in untreated cells (**Fig. 4c**), we identified the most differentially regulated genes after doxorubicin treatment between DOX and DOXTOX hiPSC-CMs (**Fig. 4d** and **Supplementary Fig. 5c**). The relative activity of the gene modules previously identified in hESC-CMs was recapitulated well in the doxorubicin-treated hiPSC-CMs (**Fig. 4e** and **Supplementary Fig. 6a**,**b**).

An independent pairwise comparison of the DOX versus the DOXTOX hiPSC-CM groups at baseline and at 1 μM identified *RELA*, *NFKB1*, and *RARA* with significantly ($P < 1.8 \times 10^{-4}$) altered target gene expression, and signal transducer and activator of transcription (STAT) 3 as a significantly ($q < 5.0 \times 10^{-3}$) modulated signaling pathway between the DOX and DOXTOX hiPSC-CM groups; these genes and pathway have been previously described to be involved in DIC[41,42] (**Supplementary Table 5**). In addition, as compared to the untreated DOXTOX hiPSC-CMs, DOXTOX hiPSC-CMs treated with 1 μM doxorubicin showed significantly ($q < 1.3 \times 10^{-2}$) increased expression of programmed cell death and p53 downstream pathway genes, and target genes encoding transcription factors—including *TP53*, *BRCA1* (encoding breast cancer 1), *PALB2* (encoding partner and localizer of *BRCA2*), *STAT3*, *CEBPA* (encoding CCAAT/enhancer binding protein alpha), and *PPARG* (encoding PPAR gamma). There was a significant ($q < 1.3 \times 10^{-2}$) decrease in the expression of genes involved in muscle contraction, cholesterol biosynthesis, and anatomical structure development, and in the expression of the target genes *SUZ12* (encoding SUZ12 polycomb repressive complex 2 subunit), *CTBP2* (encoding C-terminal binding protein 2), *EPAS1* (encoding endothelial PAS domain protein 1), and *RAD21* (encoding RAD21 cohesin complex component) (**Fig. 4f**, **Supplementary Fig. 6c** and **Supplementary Table 6**). Extrapolating exon sequence information from the RNA-seq data, we analyzed coding sequence variants in the *BRCA1*, *BRCA2*, and *PALB2* genes and found that homozygous, non-synonymous variants in *BRCA1* were present in the DOXTOX subjects (**Supplementary Note**). It has previously been demonstrated that germline *BRCA1* mutations may be associated with DIC[43].

We next examined the expression of genes identified by PharmGKB to be associated with DIC[40]. Genes differentially expressed between the DOX and DOXTOX hiPSC-CM populations include those associated with redox cycling of doxorubicin and production of ROS (such as NAD(P)H dehydrogenase, quinone 2; *NQO2*) and the generation of reactive nitrogen species (such as nitric oxide synthase 3; *NOS3*), as well as genes encoding antioxidants (such as superoxide

© 2016 Nature America, Inc. All rights reserved.

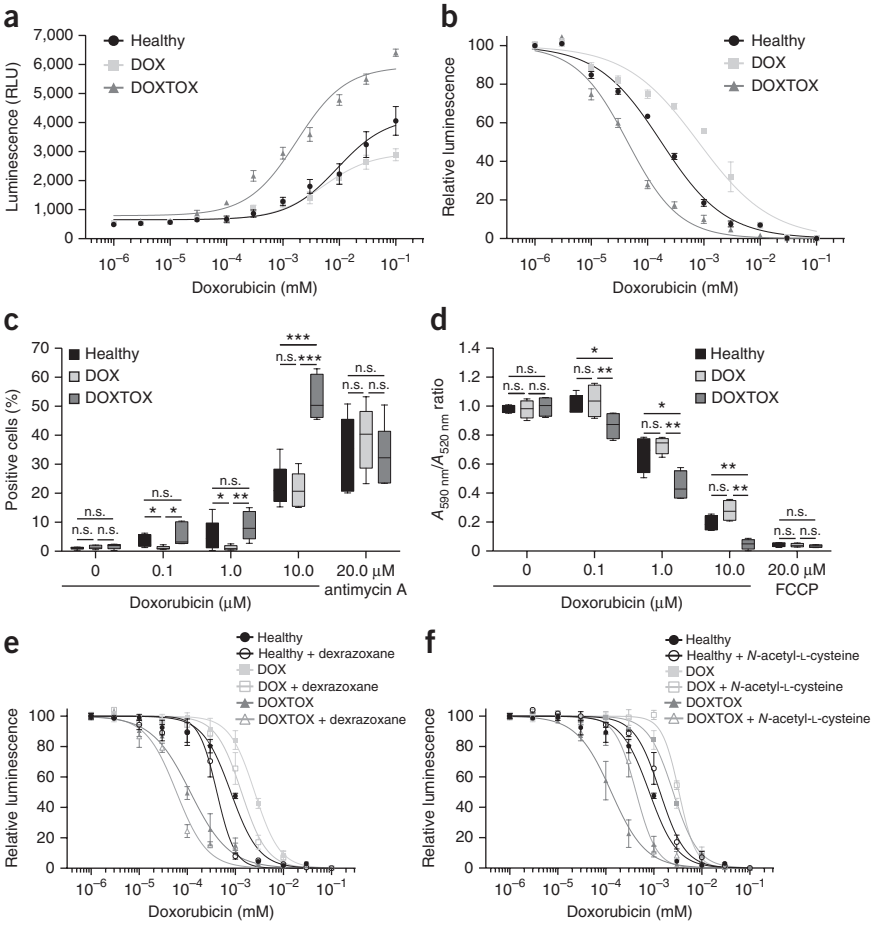

Figure 3 The effects of doxorubicin on oxidative stress in patient-specific hiPSC-CMs. (**a**–**d**) The effects of doxorubicin treatment for 24 h on hydrogen peroxide (H_2O_2) (**a**), antioxidant glutathione (GSH) (**b**), and mitochondrial superoxide (**c**) levels, and on mitochondrial membrane potential (**d**). In **c**, treatment with antimycin A, which inhibits ATP production and results in the formation of mitochondrial superoxides, was used as a positive control. In **d**, treatment with FCCP, which disrupts $\Delta_{\psi m}$, was used as a positive control. In **a**,**b**, the data were obtained using hiPSC-CMs from four patients per group, one cell line per patient, the assay was repeated twice ($n = 8$). In **c**,**d**, the data were obtained using hiPSC-CMs from four patients per group, one cell line per patient ($n = 4$). RLU, relative luminescence units. (**e**,**f**) Effects of a 72-h doxorubicin treatment on cell viability in the presence or absence of either the iron chelator dexrazoxane (DRZ) (**e**) or the antioxidant NAC (**f**), as assessed using an ATP-based cell-viability assay. The data were obtained using hiPSC-CMs from four patients per group, one cell line per patient ($n = 4$). Throughout, data are represented as mean ± s.e.m. $^*P < 0.05$; $^{**}P < 0.01$; $^{***}P < 0.005$; n.s., not significant; by unpaired two-tailed Student's *t*-test.

dismutase 3; *SOD3*), although there was no effect on catalase (*CAT*) expression[44] (**Fig. 5a** and **Supplementary Fig. 7a**,**b**). We also found a significant ($P < 0.05$) effect on calpain 6 (*CAPN6*) expression, whose product is involved in the Ca^{2+}-overload response[30], although we noted no differences in the expression of other calcium-handling protein–encoding genes (**Supplementary Fig. 7c**). Downregulation of cardiac structural gene expression in response to doxorubicin is well established[28,45], and we confirmed that doxorubicin treatment led to downregulation of myosin, heavy chain 7, cardiac muscle, beta (*MYH7*) and troponin I3, cardiac type (*TNNI3*), among other such transcripts, in both cell populations (**Fig. 5b** and **Supplementary Fig. 7d**). Additionally, we found significant ($P < 0.05$) differences in the expression of genes involved in iron transport and storage[34] (**Supplementary Fig. 7e**), of the chromatin remodeling and chemotherapy-resistance-related gene SWI/SNF related, matrix associated, actin dependent regulator of chromatin, subfamily a, member 4 (*SMARCA4*)[46] (**Supplementary Fig. 7f**), and of genes involved in apoptosis[42] (**Fig. 5b** and **Supplementary Fig. 7g**), as well as in genes previously identified by DIC genome-wide association studies (GWAS) and by targeted absorption, distribution, metabolism, and excretion (ADME) single-nucleotide polymorphism (SNP) association studies[47] (**Supplementary Fig. 7h**). After doxorubicin treatment, *PPARGC1A* expression was downregulated to a smaller extent in DOXTOX cells than in DOX cells. Finally, there were significant ($P < 0.01$) effects of doxorubicin treatment on the expression of *STAT1*, *STAT3*, *BRCA1*, and *BRCA2* (**Fig. 5b** and **Supplementary Fig. 7i**).

Differences in patient-specific mitochondrial function

Because mitochondrial function has been identified as a key component of DIC[48], we next performed a baseline (i.e., without any doxorubicin treatment) mitochondrial stress test in DOX and DOXTOX hiPSC-CMs, using a Seahorse XF24 extracellular-flux analyzer (**Fig. 5c**). We observed more extreme reductions in basal and maximal respiration in DOXTOX hiPSC-CMs than in DOX hiPSC-CMs after doxorubicin treatment, particularly with 1 μM and 10 μM doxorubicin (**Supplementary Fig. 8a**–**d**). Notably, even without doxorubicin treatment, we observed differences between these two cell populations in basal respiration, maximal mitochondrial respiration, and spare respiratory capacity, as assessed by subjecting cells to carbonyl cyanide-*4*-(trifluoromethoxy) phenylhydrazone (FCCP), which promotes dissipation of $\Delta_{\psi m}$ and leads to an increase in oxygen consumption that is accompanied by a decrease in ATP synthesis (**Fig. 5d**). To further evaluate this result, we assessed baseline ATP levels, which were significantly ($P < 0.01$) lower in DOXTOX hiPSC-CMs than in DOX or healthy hiPSC-CMs (**Fig. 5e**). The amounts of proteins involved in oxidative phosphorylation, as assessed by immunoblotting, showed a similar trend (**Fig. 5f** and **Supplementary Fig. 8e**), as did quantification of citrate synthase activity, a marker of mitochondrial content (**Fig. 5g**). We next measured the ratio of nuclear to mitochondrial DNA to estimate mitochondrial content and found that DOXTOX hiPSC-CMs had 30.1 ± 2.4% less mitochondrial content than DOX hiPSC-CMs (**Fig. 5h**). To determine whether this effect was generalizable to other cell types, we assessed mitochondrial content in patient fibroblasts and undifferentiated hiPSCs but did not find significant differences (**Fig. 5i**,**j**). To further study whether patient-derived fibroblasts or hiPSCs could be used as cell models for predicting DIC, we also performed viability assays over a 5-log concentration

© 2016 Nature America, Inc. All rights reserved.

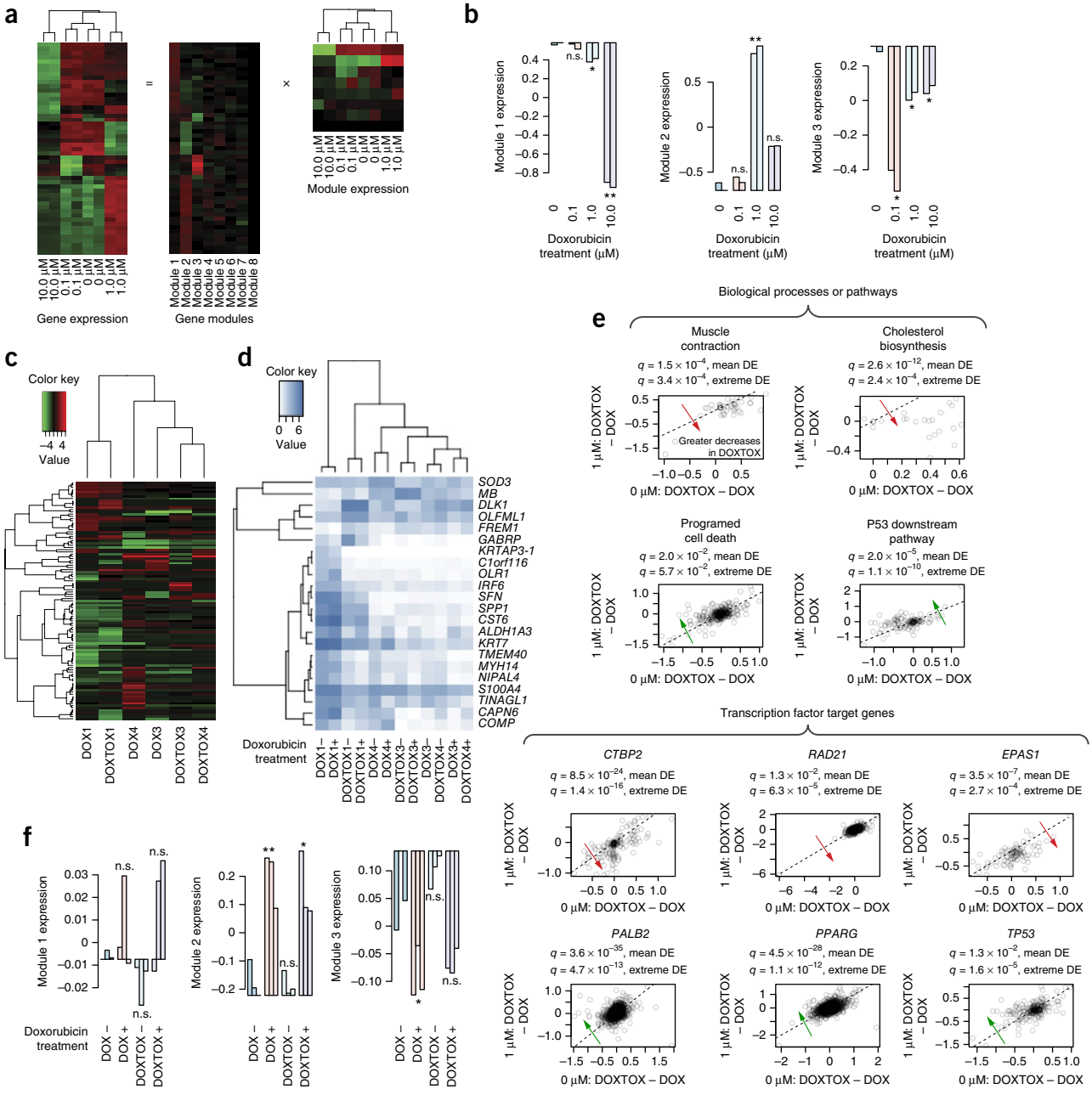

Figure 4 Modulation of gene expression in hESC-CMs and hiPSC-CMs by doxorubicin. (**a**) Decomposition of gene expression data by independent component analysis (ICA) in hESC-CM samples ($n = 2$ for each condition) treated with 0, 0.1, 1.0, or 10.0 μM of doxorubicin for 24 h. Shown on the left is the expression of the 51 most differentially regulated genes, which were used to generate eight functional gene modules of transcriptional responses following doxorubicin treatment. Matrix multiplication (×) of the independent gene modules (middle) by the mixing coefficient matrix (right) reconstructs (=) the original gene expression matrix (left). A linear combination of multiple statistically independent gene modules is illustrated (right). (**b**) Gene modules significantly associated with doxorubicin treatment at the indicated concentrations for hESC-CMs. Consensus functions of genes in the models: module 1, oxidation and hypoxia stress response and enrichment of genes related to heart morphogenesis; module 2, inflammation and DNA damage repair; and module 3, cell cycle arrest and apoptosis. (**c**) Differential gene expression in DOX and DOXTOX hiPSC lines after treatment with 1 μM doxorubicin for 24 h. The values were normalized to baseline (0 μM) expression. The data were obtained using hiPSC-CMs from three patients per group, one cell line per patient ($n = 3$); 12 RNA-seq samples total. (**d**) Heat map of the genes that are most differentially expressed between DOX and DOXTOX hiPSC-CMs after 1 μM doxorubicin treatment. (**e**) Scatter plots in which the difference in inferred transcription factor activity for biological processes or pathways (top) and transcription factor target genes (bottom) between the DOXTOX and DOX hiPSC-CM groups at 0 μM doxorubicin (x axis) versus 1 μM doxorubicin (y axis) are plotted. Systematic deviation from the diagonal (dashed line), suggesting patient-specific cell responses upon doxorubicin treatment, are shown. Green arrows signify greater increases in the DOXTOX group, and red arrows signify greater decreases in the DOXTOX group. The significance of a given gene set is evaluated in two ways—by mean differential expression (DE) and extreme DE. For mean DE, we tested whether delta-delta expression ($y - x$) has identical means for the member genes of the gene set against other genes using a Student's t-test. For extreme DE, we tested whether extreme delta-delta expression values are enriched for member genes of the gene set using Fisher's exact test. A multitest-corrected $P < 0.05$ is considered to be significant. (**f**) Expression of gene modules 1–3 in DOX and DOXTOX hiPSC-CMs treated with 1 μM doxorubicin. Throughout, data are represented as mean ± s.e.m. $^*P < 0.05$; $^{**}P < 0.01$; $^{***}P < 0.005$; n.s., not significant.

© 2016 Nature America, Inc. All rights reserved.

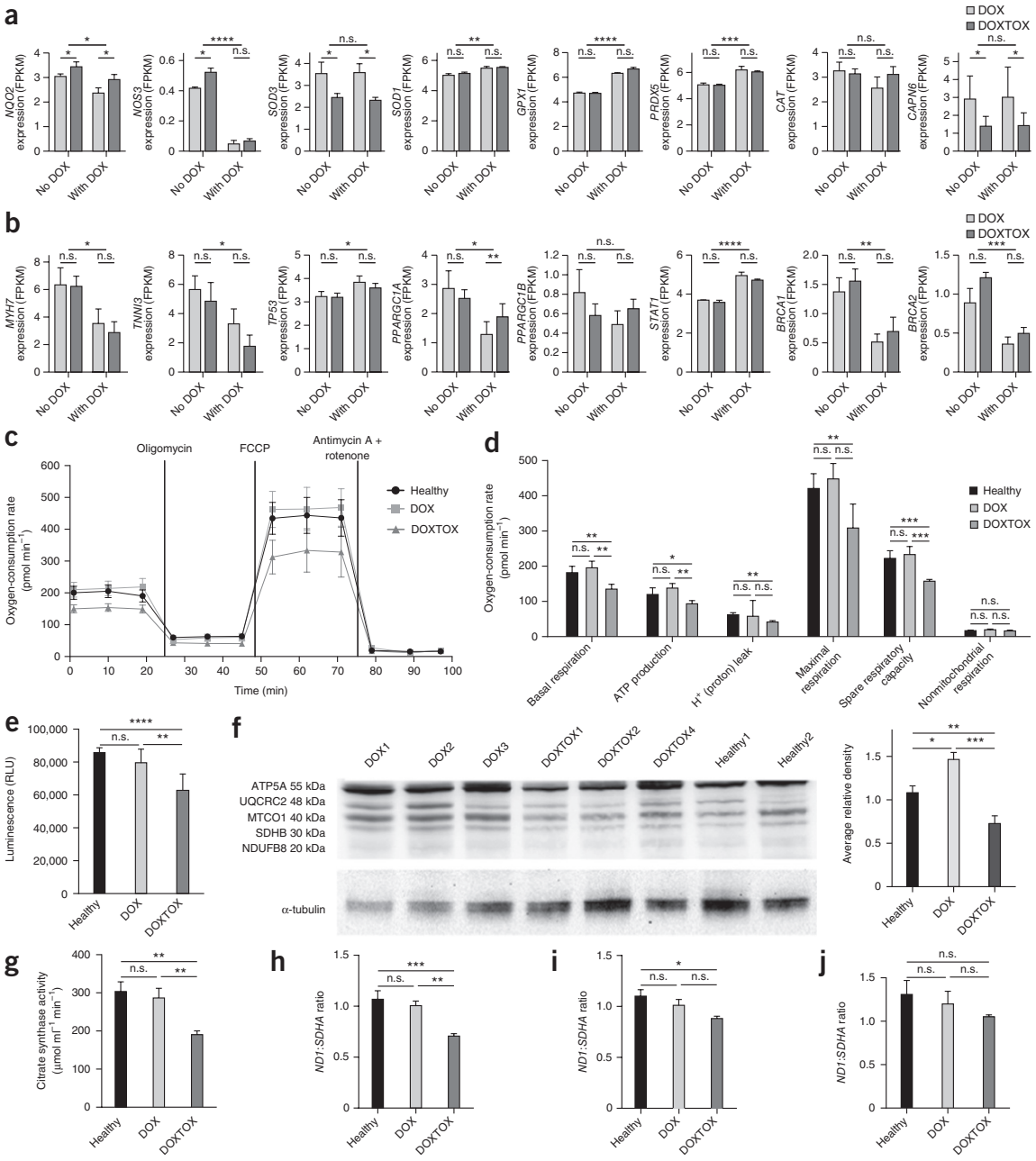

Figure 5 Assessment of baseline mitochondrial function in patient-specific hiPSC-CMs. (**a**) Expression of ROS-related (*NQO2*, *NOS3*, *SOD3*, *SOD1*, *GPX1*, *PRDX5*, and *CAT*) and calcium-overload-related (*CAPN6*) genes in DOX and DOXTOX hiPSC-CMs without or with doxorubicin treatment (1 μM for 24 h). The data were obtained by using hiPSC-CMs from three patients per group, one cell line per patient ($n = 3$ per condition). (**b**) Expression of sarcomeric protein genes (*MYH7* and *TNNI3*), the apoptosis-related gene *TP53*, genes related to *TOP2B* expression (*PPARGC1A* and *PPARGC1B*), the transcription-factor-encoding gene *STAT1*, and the breast-cancer-related *BRCA1* and *BRCA2* genes in DOX and DOXTOX hiPSC-CMs without or with doxorubicin treatment (1 μM for 24 h). The data were obtained by using hiPSC-CMs from three patients per group, one cell line per patient ($n = 3$ per condition). In **a**,**b**, error bars represent s.e.m. $^*P < 0.05$; $^{**}P < 0.01$; $^{***}P < 0.005$; $^{****}P < 0.001$; n.s., not significant; by two-way ANOVA (no doxorubicin versus with doxorubicin treatment) or Student's *t*-test (DOX versus DOXTOX). (**c**) Representative Seahorse extracellular-flux assays measuring oxygen-consumption rate (OCR). The data were obtained by using hiPSC-CMs from four patients per group, one cell line per patient ($n = 3$ per condition). (**d**) Analysis of Seahorse extracellular-flux assay results. The data were obtained using hiPSC-CMs from four patients per group, one cell line per patient, and the assay was repeated three times ($n = 12$ per condition). (**e**) Quantification of ATP levels in hiPSC-CMs. The data were obtained by using hiPSC-CMs from four patients per group, one cell line per patient, and the assay was repeated twice ($n = 8$); 100,000 cells per sample were assayed. (**f**) Western blot analysis for selected proteins involved in oxidative phosphorylation (NDUFB8 (complex I); SDHB (complex II); UQCRC2 (complex III); MTCO1 (complex IV); ATP5A (complex V)) (left) and quantification of average band densities for all five proteins (right) ($n = 3$ for DOX and DOXTOX; $n = 2$ for healthy). (**g**) Citrate synthase assay, as a marker of mitochondrial content, in hiPSC-CMs ($n = 8$ per group). Each bar shows the average value of four cell lines with two experimental replicates per cell line (5×10^6 cells per sample). (**h**–**j**) Quantification of the ratio of mitochondria-encoded complex I *ND1* DNA to nuclear-encoded complex II *SDHA* DNA in healthy control, DOX, and DOXTOX hiPSC-CMs ($n = 4$ cell lines per group) (**h**), patient-derived fibroblasts ($n = 4$ cell lines per group) (**i**), and patient-derived hiPSCs ($n = 4$ cell lines per group) (**j**). Throughout, data are represented as mean ± s.e.m. Unless noted, $^*P < 0.05$; $^{**}P < 0.01$; $^{***}P < 0.005$; $^{****}P < 0.001$; n.s., not significant; by paired two-tailed Student's *t*-test.

© 2016 Nature America, Inc. All rights reserved.

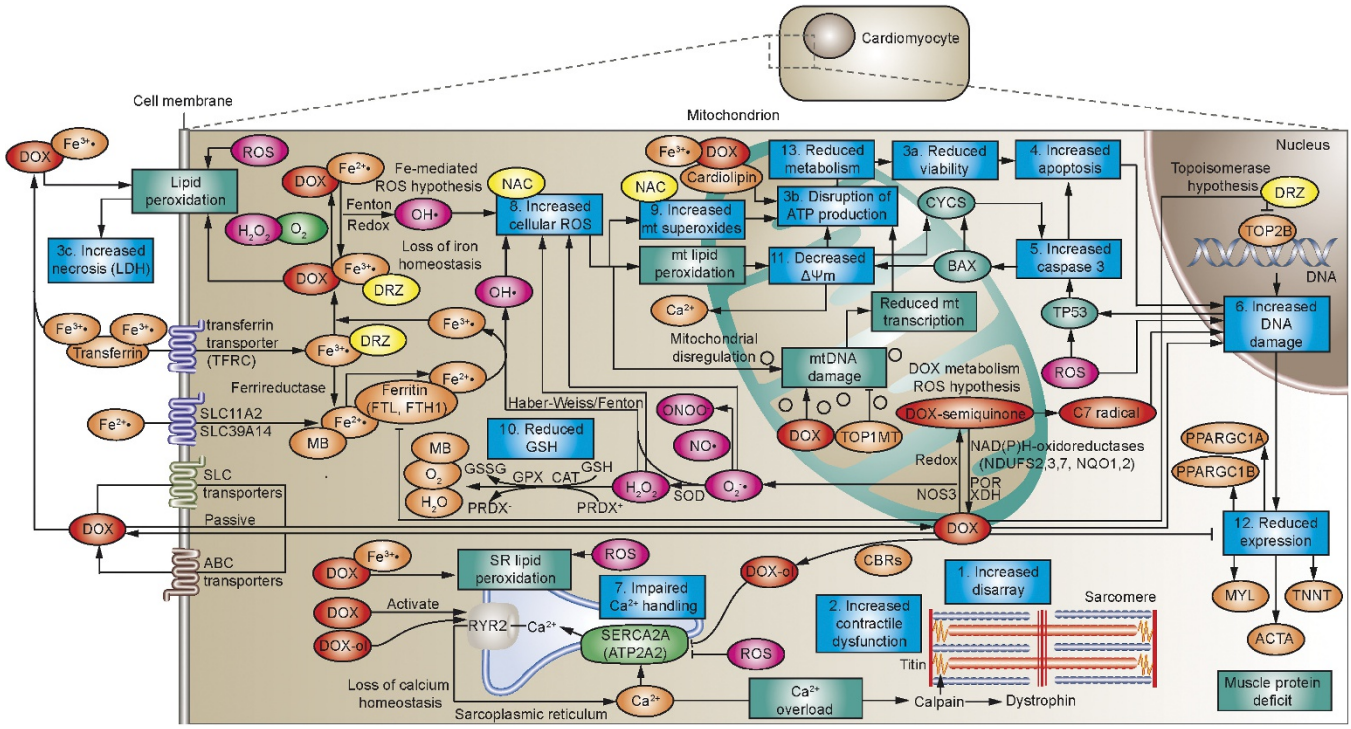

Figure 6 Schematic of the effects of doxorubicin on patient-specific hiPSC-CMs in relationship to established DIC pathways. The numbered cyan boxes demonstrate our findings, with statements describing the effects of doxorubicin on DOXTOX hiPSC-CMs, as compared to its effects on DOX hiPSC-CMs. Doxorubicin (DOX), doxorubinol (DOX-ol), doxorubicin-semiquinone (DOX-semiquinone), C7-centered radical aglycone (C7 radical), nitric oxide synthase 3 (NOS3), NADH dehydrogenases (collectively NAD(P)H oxidoreductases), P450 (cytochrome) oxidoreductase (POR), xanthine oxidase (XDH) superoxide radical (O_2^-•), hydrogen peroxide (H_2O_2), hydroxyl radical (OH•), nitric oxide (NO•), peroxynitrite ($ONOO^-$), superoxide dismutase (SOD), catalase (CAT), glutathione (GSH), glutathione peroxide (GPX), glutathione disulfide (GSSG), peroxiredoxin (PRDX), myoglobin (MB), ferrous iron (Fe^{2+}), ferric iron (Fe^{3+}), dexrazoxane (DRZ), *N*-acetyl-L-cysteine (NAC), topoisomerase (DNA) 1 mitochondrial (TOP1MT), BCL2-associated X protein (BAX), cytochrome *c* (CYCS), tumor protein p53 (TP53), topoisomerase 2B (TOP2B), ryanodine receptor 2 (RYR2), ATPase, Ca^{2+} transporting, cardiac muscle slow twitch 2 (ATP2A2), myosin light chain (MYL), cardiac troponin T (TNNT), α-actinin (ACTA), peroxisome proliferator-activated receptor gamma coactivator 1-α (PPARGC1A), and peroxisome proliferator-activated receptor gamma coactivator 1-β (PPARGC1B).

range of doxorubicin. In contrast to our results with hiPSC-CMs, we found that these cell types could not recapitulate the patient response to doxorubicin (**Supplementary Fig. 9**).

DISCUSSION

Our results suggest that hiPSC-CMs can recapitulate the patient-specific predilection to DIC and enable the prediction of clinical susceptibilities of high-risk populations to drug-induced cardiotoxicity. Differences in the response of DOX and DOXTOX hiPSC-CMs to doxorubicin are evident in multiple processes relevant to DIC (**Fig. 6**), such that this cell model recapitulates numerous DIC phenotypes shown in animal models, particularly with respect to ROS pathways and mitochondrial dysregulation[33,49]. Although the effects of doxorubicin treatment on a pure population of cardiomyocytes *in vitro* may not mimic all of the processes that occur *in vivo,* it should be noted that the differences observed between DOX and DOXTOX hiPSC-CMs were not observed using other patient-derived cell types, such as fibroblasts or hiPSCs.

The hiPSC-CM model is not without limitations[50], including the immature phenotype of the cardiomyocytes[51], the indeterminate subtype of the cardiomyocytes[52], and the lack of other cardiac cell types, such as fibroblasts and endothelial cells[53]. Yet, these features are also a strength of the model—immature cells are easier to dissociate, pure cardiomyocytes are more suited than mixed cell populations to high-throughput plate assays and high-content imaging[54], and RNA-seq analysis is more accurate when there is no contamination with other cell types.

By using this cell model, it should be possible to validate the relevance of gene variants identified through GWAS[55,56] to DIC. This platform also holds considerable promise for the discovery of new DIC cardioprotectants[57], although our findings—that the iron chelator dexrazoxane was not cardioprotective, whereas the antioxidant NAC was—may highlight differences between a whole-animal model and an *in vitro* cardiomyocyte model. In particular, it is believed that the heart is uniquely at risk to doxorubicin toxicity owing to the high density of mitochondria in cardiomyocytes, which make up 35% of the total cell volume[58]. In hiPSC-CMs, however, mitochondrial density is lower[59], and confirmation of this 'mitochondrial content' risk factor will require further analysis. Finally, interpretation of our findings that show variation of basal metabolism in hiPSC-CMs needs to take into account that each of the cell types studied (hiPSC-CMs, fibroblasts, and hiPSCs) was derived from patients who had already been treated with doxorubicin; thus, any systemic damage to the nuclear or mitochondrial DNA in the original patient fibroblasts used for reprogramming may have been carried over to the hiPSCs and hiPSC-CMs. A better approach might be to study hiPSCs derived from fibroblasts obtained before doxorubicin treatment. Although this approach would require a substantially larger, longitudinal patient study, such a study could help realize the goal of precision medicine for cardio-oncology.

© 2016 Nature America, Inc. All rights reserved.

METHODS

Methods and any associated references are available in the online version of the paper.

Accession codes. Gene Expression Omnibus: RNA-seq data have been deposited with accession code GSE76314. Microarray data have been deposited with the accession code GSE79413.

Note: Any Supplementary Information and Source Data files are available in the online version of the paper.

ACKNOWLEDGMENTS

We thank J. Odegaard for analysis of teratoma slides. This work was supported by the US National Institutes of Health (NIH) grants K99/R00 HL121177 (P.W.B.), R21 HL123655 (D.B.), R01 LM05652 (R.B.A.), R01 GM102365 (R.B.A.), R24 GM61374 (R.B.A.), R01 HL123968 (J.C.W.), R01 HL126527 (J.C.W.), R01 HL128170 (J.C.W.), R01 HL130020 (J.C.W.), R01 AR063963 (H.M.B.), R01 AG020961 (H.M.B.), R21 AG04481501 (H.M.B.), and R01 NS089533 (H.M.B.); the American Heart Association (AHA) grants AHA 14BGIA20480329 (P.W.B.), AHA 13POST14480004 (A.C.C.), and AHA 13EIA14420025 (J.C.W.); a Dixon Translational Research Grant Young Investigator Award (P.W.B.), the California Institute of Regenerative Medicine (CIRM) awards IT1-06596 (J.C.W.), TR3-05501 (H.M.B.) and RB5-07469 (H.M.B.); the Muscular Dystrophy Association grant 4320 (H.M.B.); the Baxter Foundation (H.M.B.); and a Burroughs Wellcome Fund Innovation in Regulatory Science Award (J.C.W.).

AUTHOR CONTRIBUTIONS

P.W.B. performed project planning, experimental design, hiPSC reprogramming, cell culture, characterizations, differentiation, cardiotoxicity analysis, flow cytometry, data analysis, and wrote the manuscript; Y.F.L. performed computational analyses of microarray and RNA-seq data, gene enrichment analysis, and wrote part of the manuscript; E.M. and A.H. performed cell culture; E.M. and A.S. performed immunohistochemistry; H.W. performed Ca^{2+} imaging; P.W.B., S.-G.O., A.C.C., M.J.C., and A.D.E. performed Seahorse analysis; S.-G.O. performed mitochondrial analysis; J.W.K., M.L.T., and R.M.W. recruited patients; H.M.B., D.B., R.B.A., and J.C.W. helped in manuscript preparation; J.C.W. and P.W.B. provided conceptual design of the study and funding support.

COMPETING FINANCIAL INTERESTS

The authors declare competing financial interests: details are available in the online version of the paper.

Reprints and permissions information is available online at http://www.nature.com/reprints/index.html.

1. Lipshultz, S.E., Franco, V.I., Miller, T.L., Colan, S.D. & Sallan, S.E. Cardiovascular disease in adult survivors of childhood cancer. *Annu. Rev. Med.* **66**, 161–176 (2015).
2. Giordano, S.H., Lin, Y.-L., Kuo, Y.F., Hortobagyi, G.N. & Goodwin, J.S. Decline in the use of anthracyclines for breast cancer. *J. Clin. Oncol.* **30**, 2232–2239 (2012).
3. Lefrak, E.A., Pitha, J., Rosenheim, S. & Gottlieb, J.A. A clinicopathologic analysis of Adriamycin cardiotoxicity. *Cancer* **32**, 302–314 (1973).
4. Von Hoff, D.D. *et al.* Risk factors for doxorubicin-induced congestive heart failure. *Ann. Intern. Med.* **91**, 710–717 (1979).
5. Swain, S.M., Whaley, F.S. & Ewer, M.S. Congestive heart failure in patients treated with doxorubicin: a retrospective analysis of three trials. *Cancer* **97**, 2869–2879 (2003).
6. Kremer, L.C.M., van der Pal, H.J.H., Offringa, M., Van Dalen, E.C. & Voûte, P.A. Frequency and risk factors of subclinical cardiotoxicity after anthracycline therapy in children: a systematic review. *Ann. Oncol.* **13**, 819–829 (2002).
7. Shakir, D.K. & Rasul, K.I. Chemotherapy-induced cardiomyopathy: pathogenesis, monitoring, and management. *J. Clin. Med. Res.* **1**, 8–12 (2009).
8. Bernstein, D. & Burridge, P. Patient-specific pluripotent stem cells in doxorubicin cardiotoxicity: a new window into personalized medicine. *Prog. Pediatr. Cardiol.* **37**, 23–27 (2014).
9. Lipshultz, S.E., Cochran, T.R., Franco, V.I. & Miller, T.L. Treatment-related cardiotoxicity in survivors of childhood cancer. *Nat. Rev. Clin. Oncol.* **10**, 697–710 (2013).
10. Granger, C.B. Prediction and prevention of chemotherapy-induced cardiomyopathy: can it be done? *Circulation* **114**, 2432–2433 (2006).
11. Deavall, D.G., Martin, E.A., Horner, J.M. & Roberts, R. Drug-induced oxidative stress and toxicity. *J. Toxicol.* **2012**, 645460 (2012).
12. Zhang, S. *et al.* Identification of the molecular basis of doxorubicin-induced cardiotoxicity. *Nat. Med.* **18**, 1639–1642 (2012).
13. Khiati, S. *et al.* Mitochondrial topoisomerase I (Top1mt) is a novel limiting factor of doxorubicin cardiotoxicity. *Clin. Cancer Res.* **20**, 4873–4881 (2014).
14. Hanna, A.D., Lam, A., Tham, S., Dulhunty, A.F. & Beard, N.A. Adverse effects of doxorubicin and its metabolic product on cardiac RyR2 and SERCA2A. *Mol. Pharmacol.* **86**, 438–449 (2014).
15. Goormaghtigh, E., Brasseur, R., Huart, P. & Ruysschaert, J.M. Study of the Adriamycin–cardiolipin complex structure using attenuated total-reflection infrared spectroscopy. *Biochemistry* **26**, 1789–1794 (1987).
16. Ichikawa, Y. *et al.* Cardiotoxicity of doxorubicin is mediated through mitochondrial iron accumulation. *J. Clin. Invest.* **124**, 617–630 (2014).
17. Holmberg, S.R. & Williams, A.J. Patterns of interaction between anthraquinone drugs and the calcium-release channel from cardiac sarcoplasmic reticulum. *Circ. Res.* **67**, 272–283 (1990).
18. Burridge, P.W. *et al.* Modeling cardiovascular diseases with patient-specific human pluripotent stem cell–derived cardiomyocytes. *Methods Mol. Biol.* **1353**, 119–130 (2016).
19. Cahan, P. & Daley, G.Q. Origins and implications of pluripotent stem cell variability and heterogeneity. *Nat. Rev. Mol. Cell Biol.* **14**, 357–368 (2013).
20. Peterson, S.E. & Loring, J.F. Genomic instability in pluripotent stem cells: implications for clinical applications. *J. Biol. Chem.* **289**, 4578–4584 (2014).
21. Burridge, P.W. *et al.* Chemically defined generation of human cardiomyocytes. *Nat. Methods* **11**, 855–860 (2014).
22. Burridge, P.W., Holmström, A. & Wu, J.C. Chemically defined culture and cardiomyocyte differentiation of human pluripotent stem cells. *Curr. Protoc. Hum. Genet.* **87**, 21.3 (2015).
23. Rana, P., Anson, B., Engle, S. & Will, Y. Characterization of human induced pluripotent stem cell–derived cardiomyocytes: bioenergetics and utilization in safety screening. *Toxicol. Sci.* **130**, 117–131 (2012).
24. Yang, X. *et al.* Triiodo-L-thyronine promotes the maturation of human cardiomyocytes derived from induced pluripotent stem cells. *J. Mol. Cell. Cardiol.* **72**, 296–304 (2014).
25. Robert, J. *et al.* Comparative pharmacokinetics and metabolism of doxorubicin and epirubicin in patients with metastatic breast cancer. *Cancer Treat. Rep.* **69**, 633–640 (1985).
26. Bramwell, V.H.C. *et al.* Safety and efficacy of the multidrug-resistance inhibitor biricodar (VX-710) with concurrent doxorubicin in patients with anthracycline-resistant advanced soft tissue sarcoma. *Clin. Cancer Res.* **8**, 383–393 (2002).
27. Berdichevski, A. *et al.* TVP1022 protects neonatal rat ventricular myocytes against doxorubicin-induced functional derangements. *J. Pharmacol. Exp. Ther.* **332**, 413–420 (2010).
28. Ito, H. *et al.* Doxorubicin selectively inhibits muscle gene expression in cardiac muscle cells *in vivo* and *in vitro*. *Proc. Natl. Acad. Sci. USA* **87**, 4275–4279 (1990).
29. Ruan, Y. *et al.* SIRT1 suppresses doxorubicin-induced cardiotoxicity by regulating the oxidative stress and p38MAPK pathways. *Cell. Physiol. Biochem.* **35**, 1116–1124 (2015).
30. Lim, C.C. *et al.* Anthracyclines induce calpain-dependent titin proteolysis and necrosis in cardiomyocytes. *J. Biol. Chem.* **279**, 8290–8299 (2004).
31. Chen, B. *et al.* Disruption of a GATA4–ANKRD1 signaling axis in cardiomyocytes leads to sarcomere disarray: implications for anthracycline cardiomyopathy. *PLoS One* **7**, e35743 (2012).
32. Doroshow, J.H. Effect of anthracycline antibiotics on oxygen radical formation in rat heart. *Cancer Res.* **43**, 460–472 (1983).
33. Shi, Y., Moon, M., Dawood, S., McManus, B. & Liu, P.P. Mechanisms and management of doxorubicin cardiotoxicity. *Herz* **36**, 296–305 (2011).
34. Xu, X., Persson, H.L. & Richardson, D.R. Molecular pharmacology of the interaction of anthracyclines with iron. *Mol. Pharmacol.* **68**, 261–271 (2005).
35. Venditti, P., Balestrieri, M., De Leo, T. & Di Meo, S. Free radical involvement in doxorubicin-induced electrophysiological alterations in rat papillary muscle fibers. *Cardiovasc. Res.* **38**, 695–702 (1998).
36. Swain, S.M. *et al.* Cardioprotection with dexrazoxane for doxorubicin-containing therapy in advanced breast cancer. *J. Clin. Oncol.* **15**, 1318–1332 (1997).
37. Deng, S. *et al.* The catalytic topoisomerase II inhibitor dexrazoxane induces DNA breaks, ATF3, and the DNA damage response in cancer cells. *Br. J. Pharmacol.* **172**, 2246–2257 (2015).
38. Farshid, A.A. *et al.* Effects of histidine and *N*-acetylcysteine on doxorubicin-induced cardiomyopathy in rats. *Cardiovasc. Toxicol.* **14**, 153–161 (2014).
39. Engreitz, J.M., Daigle, B.J. Jr., Marshall, J.J. & Altman, R.B. Independent component analysis: mining microarray data for fundamental human gene expression modules. *J. Biomed. Inform.* **43**, 932–944 (2010).
40. Thorn, C.F. *et al.* Doxorubicin pathways: pharmacodynamics and adverse effects. *Pharmacogenet. Genomics* **21**, 440–446 (2011).
41. Hussner, J. *et al.* Regulation of interferon-inducible proteins by doxorubicin via interferon-γ–Janus tyrosine kinase–signal transducer and activator of transcription signaling in tumor cells. *Mol. Pharmacol.* **81**, 679–688 (2012).
42. Zhu, W., Zhang, W., Shou, W. & Field, L.J. p53 inhibition exacerbates late-stage anthracycline cardiotoxicity. *Cardiovasc. Res.* **103**, 81–89 (2014).
43. Arts-de Jong, M., Maas, A.H.E.M., Massuger, L.F., Hoogerbrugge, N. & de Hullu, J.A. *BRCA1/2* mutation carriers are potentially at higher cardiovascular risk. *Crit. Rev. Oncol. Hematol.* **91**, 159–171 (2014).
44. Doroshow, J.H., Locker, G.Y. & Myers, C.E. Enzymatic defenses of the mouse heart against reactive oxygen metabolites: alterations produced by doxorubicin. *J. Clin. Invest.* **65**, 128–135 (1980).

© 2016 Nature America, Inc. All rights reserved.

45. Torti, S.V., Akimoto, H., Lin, K., Billingham, M.E. & Torti, F.M. Selective inhibition of muscle gene expression by oxidative stress in cardiac cells. *J. Mol. Cell. Cardiol.* **30**, 1173–1180 (1998).
46. Naidu, S.R., Love, I.M., Imbalzano, A.N., Grossman, S.R. & Androphy, E.J. The SWI/SNF chromatin remodeling subunit BRG1 is a critical regulator of p53 necessary for proliferation of malignant cells. *Oncogene* **28**, 2492–2501 (2009).
47. Visscher, H. *et al.* CPNDS Consortium. Validation of variants in *SLC28A3* and *UGT1A6* as genetic markers predictive of anthracycline-induced cardiotoxicity in children. *Pediatr. Blood Cancer* **60**, 1375–1381 (2013).
48. Lebrecht, D., Kokkori, A., Ketelsen, U.-P., Setzer, B. & Walker, U.A. Tissue-specific mtDNA lesions and radical-associated mitochondrial dysfunction in human hearts exposed to doxorubicin. *J. Pathol.* **207**, 436–444 (2005).
49. Octavia, Y. *et al.* Doxorubicin-induced cardiomyopathy: from molecular mechanisms to therapeutic strategies. *J. Mol. Cell. Cardiol.* **52**, 1213–1225 (2012).
50. Denning, C. *et al.* Cardiomyocytes from human pluripotent stem cells: from laboratory curiosity to industrial biomedical platform. *Biochim. Biophys. Acta* http://dx.doi:10.1016/j.bbamcr.2015.10.014 (2015).
51. Zhu, R. *et al.* Physical developmental cues for the maturation of human pluripotent stem cell–derived cardiomyocytes. *Stem Cell Res. Ther.* **5**, 117 (2014).
52. David, R. & Franz, W.M. From pluripotency to distinct cardiomyocyte subtypes. *Physiology (Bethesda)* **27**, 119–129 (2012).
53. Mathur, A. *et al.* Human iPSC-based cardiac microphysiological system for drug-screening applications. *Sci. Rep.* **5**, 8883 (2015).
54. Mercola, M., Colas, A. & Willems, E. Induced pluripotent stem cells in cardiovascular drug discovery. *Circ. Res.* **112**, 534–548 (2013).
55. Brown, S.-A., Sandhu, N. & Herrmann, J. Systems biology approaches to adverse drug effects: the example of cardio-oncology. *Nat. Rev. Clin. Oncol.* **12**, 718–731 (2015).
56. Aminkeng, F. *et al.* A coding variant in *RARG* confers susceptibility to anthracycline-induced cardiotoxicity in childhood cancer. *Nat. Genet.* **47**, 1079–1084 (2015).
57. Vejpongsa, P. & Yeh, E.T.H. Prevention of anthracycline-induced cardiotoxicity: challenges and opportunities. *J. Am. Coll. Cardiol.* **64**, 938–945 (2014).
58. Kim, H.D., Kim, C.H., Rah, B.J., Chung, H.I. & Shim, T.S. Quantitative study on the relation between structural and functional properties of the hearts from three different mammals. *Anat. Rec.* **238**, 199–206 (1994).
59. Hattori, F. *et al.* Nongenetic method for purifying stem cell–derived cardiomyocytes. *Nat. Methods* **7**, 61–66 (2010).

© 2016 Nature America, Inc. All rights reserved.

ONLINE METHODS

Human induced pluripotent cell derivation. All pluripotent and reprogramming cell cultures were maintained at 37 °C in a New Brunswick Galaxy 170R humidified incubator (Eppendorf) with 5% CO_2 and 5% O_2. Primary cell and differentiation cultures were maintained at 5% CO_2 and 21% O_2. Protocols were approved by the Stanford University Human Subjects Research Institutional Review Board. With informed written consent, two 2-mm skin punch biopsies were taken from each volunteer, diced with a scalpel, and digested with 1 mg ml^{-1} collagenase IV (Life Technologies) for 2 h at 37 °C. Fibroblasts were then grown in Dulbecco's modified Eagle's medium (DMEM) with GlutaMAX (Life Technologies) supplemented with 10% FBS (FBS, US origin, Life Technologies) in 6-well plates (Greiner) coated with a 1:200 dilution of growth-factor-reduced Matrigel (9 µg cm^{-2}, Corning). Medium was changed every other day. After reaching confluence (~1 week), fibroblasts were passaged with TrypLE Express (Life Technologies) onto Matrigel-coated T225 flasks (Thermo Scientific Nunc). For Sendai virus reprogramming, early passage (p2–p3) fibroblasts were seeded at 40,000 cells/well on Synthemax II-SC (625 ng cm^{-2}, Corning)-coated[60] 6-well plates in E8 medium[61]. E8 medium was made in-house as previously described[18] and consisted of DMEM with Ham's F12 50/50 mix (10-092-CM, Corning), 20 µg ml^{-1} *E. coli*–derived recombinant human insulin (Life Technologies), 64 µg ml^{-1} L-ascorbic acid-2-phosphate sesquimagnesium salt hydrate (Sigma-Aldrich), 10.7 µg ml^{-1} *Oryza sativa*–derived recombinant human transferrin (Optiferrin, InVitria–Sigma-Aldrich), 14 ng ml^{-1} sodium selenite (Sigma-Aldrich), 100 ng ml^{-1} recombinant human fibroblast growth factor (FGF) 2 (154 amino acids; *E. coli*–derived; Peprotech), 2 ng ml^{-1} recombinant human TGF-β1 (112 amino acids; HEK293-derived; Peprotech), and 100 ng ml^{-1} heparin sodium salt (>180 U mg^{-1}, Sigma-Aldrich). After 24 h, medium was changed to fresh E8 medium and supplemented with four CytoTune-iPS Sendai Reprogramming Kit viral particle factors (Life Technologies)[62] diluted to 20% of the manufacturer's recommendations (3×10^5 cell infectious units (CIU) of each particle per well, multiplicity of infection (MOI) = 7.5). Medium was changed after 24 h and thereafter once every day. For the first 7 d, cultures were maintained in E8 medium supplemented with 100 nM hydrocortisone (Sigma-Aldrich) and 200 µM sodium butyrate (Sigma-Aldrich), to enhance reprogramming efficiency[63]. At day 7, cells were passaged with TrypLE Express and seeded onto a Synthemax II-SC–coated 6-well plate in E7N medium (E8 medium minus TGF-β1; supplemented with 200 µM sodium butyrate). 10 µM Rho kinase inhibitor (Y27632) (Biorbyt) was added for the first 24 h after passage. Medium was changed every day, and switched to E8 medium at day 20. Individual colonies with hESC-like morphology were picked onto a 12-well plate 1 colony/well) at day 17–25 and cultured in E8 medium with 10 µM Y27632 for 24 h after picking. Subsequently, cells were expanded in 6-well plates by passaging 1:1, 1:4, 1:6, 1:8, and finally 1:12 using 0.5 mM EDTA (Life Technologies) in Dulbecco's PBS (DPBS) without Ca^{2+} or Mg^{2+} (Life Technologies) for 6 min at RT. The specific hiPSC clones used for this study were: 59FSDNC3 (DOX1), 60FSDNC1 (DOX2), 64FSDNC1 (DOX3), 65FSDNC2 (DOX4), 31FSDNC14 (DOXTOX1), 40FSDNC15 (DOXTOX2), 51FSDNC18 (DOXTOX3), and 79FSDNC1 (DOXTOX4). For hESC experiments, the line H7 (WA07)[64] was used (WiCell Research Institute).

Human induced pluripotent stem cell culture. Cells were routinely maintained in E8 medium (made as above) on 1:200 growth-factor-reduced Matrigel (9 µg cm^{-2}) and passaged every 3–4 d using 0.5 mM EDTA (as above). Cell lines were used between passages 20 and 85. All cultures (primary, pluripotent, and differentiation) were maintained with 2 ml medium per 10 cm^2 of surface area, or equivalent. All cultures were routinely tested for mycoplasma using a MycoAlert Plus Kit (Lonza).

Immunofluorescence staining for pluripotency markers. For assessment of pluripotency, hiPSCs were passaged with EDTA and plated onto Synthemax II-SC–coated (625 ng cm^{-2}) Lab-Tek II 8-chamber glass slides (Thermo Scientific Nunc) in E8 medium for 3 d. For the first 24 h, E8 medium was supplemented with 10 µM Y27632. Cells were fixed with 4% paraformaldehyde (PFA) (Electron Microscopy Services) in DPBS (Life Technologies) for 10 min at RT, permeabilized with 0.1% saponin (Sigma-Aldrich) in DPBS for 20 min at RT, blocked in 3% bovine serum albumin (BSA, Sigma-Aldrich) in DPBS for 15 min at RT, and stained with monoclonal mouse IgM to TRA-1-60 (sc-21705, 1:200), monoclonal mouse IgM to TRA-1-81 (sc-21706, 1:200), monoclonal mouse IgG3 to SSEA4 (sc-21704, 1:200), monoclonal mouse IgG2b to POU5F1 (sc-5279, 1:200), monoclonal mouse IgG1 to NANOG (sc-33759, 1:200), or monoclonal mouse IgG1 to SOX2 (sc-365823, 1:200) in 0.1% saponin in DPBS overnight at 4 °C. Cells were washed and then stained with secondary antibodies: Alexa-Fluor-488-conjugated goat anti–mouse IgM or Alexa-Fluor-488-conjugated goat anti–mouse IgG3 (1:250), and Alexa-Fluor-594-conjugated goat anti–mouse IgG2b or Alexa-Fluor-594-conjugated goat anti–mouse IgG1 (1:250) (all from Life Technologies) in 0.1% saponin in DPBS for 1 h at RT in the dark. Cells were washed three times and mounted with ProLong Diamond Antifade Mountant with DAPI (Life Technologies). Slides were imaged with a DM IL LED inverted fluorescent microscope (Leica Microsystems) and a DFC550 camera (Leica Microsystems), using LAS X software, and processed using Volocity 6.0 (PerkinElmer).

Flow cytometry to assess pluripotency. For assessment of pluripotency of hiPSCs, at 3 d after passage, cells were dissociated with TrypLE Express for 3 min at 37 °C, and 1 million cells were transferred to flow cytometry tubes (BD Biosciences). Cells were then fixed with 4% PFA in DPBS for 10 min, permeabilized with 0.1% saponin (Sigma-Aldrich) in DPBS for 20 min, and stained using mouse IgM to TRA-1-81 conjugated to Alexa Fluor 488 (BD Biosciences, 560173), or mouse IgG_3 to SSEA4 conjugated to Alexa Fluor 488 (BD Biosciences 560308), mouse IgG1 to POU5F1 conjugated to Alexa Fluor 488 (BD Biosciences, 560217), or mouse IgG2a to SOX2 conjugated to Alexa Fluor 647 (BD Biosciences, 245610) at a 1:50 dilution for 30 min at RT. Isotype controls—fluorescein isothiocyante (FITC)-conjugated mouse IgM (BD Biosciences, 555583); Alexa-Fluor-488-conjugated mouse IgG3 (BD Biosciences, 563536); Alexa-Fluor-488-conjugated mouse IgG1 (BD Biosciences, 557702); and Alexa-Fluor-647-conjugated mouse IgG2a (BD Biosciences, 557715)—were used to establish gating. Cells were analyzed using a FACSAria II instrument (BD Biosciences) with a 100-µm nozzle and FACSDiva software. Data was analyzed using FlowJo X (Tree Star).

Quantitative real-time PCR. To analyze pluripotent gene expression, cells were dissociated with TrypLE Express for 5 min at 37 °C, triturated, diluted in E8 medium, and centrifuged at 200*g* for 4 min. Medium was aspirated, and cell pellets were snap-frozen in liquid nitrogen and stored at −80 °C. RNA was isolated using an RNeasy Plus kit (QIAGEN), cDNA was produced using the High-Capacity RNA-to-cDNA kit (Life Technologies), and real-time PCR was performed using the following TaqMan Gene Expression Assay (Life Technologies) primer and probe sets: 18S (Hs99999901_s1), NANOG (Hs02387400_g1), POU5F1 (Hs00999632_g1), SOX2 (Hs01053049_s1), KLF4 (Hs00358836_m1), LIN28 (Hs00702808_s1), MYC (Hs00153408_m1), UTF1 (Hs00747497_g1), ABCG2 (Hs01053790_m1), DMNT3B (Hs01002405_m1), TERT (Hs99999022_m1), and TP53 (Hs99999147_m1). Real-time PCR was performed using the TaqMan Gene Expression Master Mix and a 7900HT Real-Time PCR System (Life Technologies). All PCR reactions were performed in quadruplicate, normalized to the 18S rRNA endogenous control gene, and assessed using the comparative C_t method[5].

Teratoma analysis. For assessment of teratoma formation by hiPSCs, cells from three confluent wells were dissociated with 0.5 mM EDTA, centrifuged at 200*g* for 4 min, resuspended in 100 µl of growth-factor-reduced Matrigel, and injected into the kidney capsule of female NOD-SCID mice (NOD.CB17–*Prkdc*^{scid}/NcrCrl strain code 394, Charles River). After 4–6 weeks, teratomas were removed, fixed in 4% PFA, embedded in paraffin wax, sectioned, and hematoxylin and eosin (H&E)-stained by the Stanford Tissue Bank. Slides were imaged and analyzed by a qualified clinical pathologist. Mouse experiments were approved by the Stanford University Administrative Panel on Laboratory Animal Care (APLAC).

Single-nucleotide polymorphism karyotyping. A single well of pluripotent cells from at least passage 20 was dissociated with 0.5 mM EDTA and centrifuged at 200*g* for 4 min. The pellet was snap-frozen in liquid nitrogen and

© 2016 Nature America, Inc. All rights reserved.

stored at −80 °C. Genomic DNA was extracted from the cell pellets using a Blood and Tissue DNA extraction kit (QIAGEN) following the manufacturer's directions. SNP karyotyping was performed using a Genome-Wide CytoScan HD Array (Affymetrix) covering 2.7 million markers and 750,000 SNPs, and analysis was done by using Chromosome Analysis Suite (ChAS, Affymetrix).

Cardiac differentiation of hiPSCs. hiPSCs (>p20) were split at 1:12 to 1:15 ratios using EDTA as described above and grown for 3–4 d, at which time they reached ~75% confluence. Medium was changed to CDM3 (chemically defined medium, three components)[6], which consists of RPMI 1640 (10-040-CM, Corning), 500 μg ml^{-1} *Oryza sativa*–derived recombinant human albumin (Oryzogen Sciencell), and 213 μg ml^{-1} L-ascorbic acid 2-phosphate (Sigma-Aldrich). Medium was changed every other day (48 h). For days 0–2, medium was supplemented with 6 μM of the glycogen synthase kinase 3-β inhibitor CHIR99021 (MedChem Express)[21,22]. On day 2, medium was changed to CDM3 supplemented with 2 μM of the Wnt inhibitor Wnt-C59 (Biorbyt). Medium was changed on day 4 and every other day for CDM3 cultures. Contracting cells were noted from day 7. At day 10, medium was changed to CDM3L, which consists of RPMI 1640 no glucose (11879-020, Life Technologies), 500 μg ml^{-1} recombinant human albumin, and 213 μg ml^{-1} L-ascorbic acid 2-phosphate supplemented with 4 mM L-lactic acid (Sigma-Aldrich). At day 15, medium was changed to CDM3M, which consists of RPMI 1640 no glucose, 500 μg ml^{-1} recombinant human albumin, 213 μg ml^{-1} L-ascorbic acid 2-phosphate supplemented with 10 mM D-galactose (Sigma-Aldrich)[23], 4 mM L-lactic acid, 1 mM sodium pyruvate (Life Technologies), 20 μg ml^{-1} insulin (Life Technologies), 1× chemically defined lipid concentrate (Life Technologies), and 200 ng ml^{-1} triiodo-L-thyronine (Sigma-Aldrich)[24].

Immunofluorescent staining for cardiomyocyte markers. Cells at differentiation day 15 were dissociated using TrypLE Express for 10 min at 37 °C, triturated, centrifuged at 200*g* for 4 min, plated onto Synthemax II-SC–coated (625 ng cm^{-2}) coverslips in CDM3 and allowed to adhere for 3–5 d. Cells were then processed as described above and stained with monoclonal mouse IgG1 to TNNT2 (13-11, Thermo Scientific, MA5-12960; 1:200), polyclonal rabbit IgG to ACTN2 (α-actinin; H-300, Santa Cruz Biotechnology, sc-15336; 1:200), monoclonal rabbit IgG to P4HB (Abcam, ab137110; 1:50), polyclonal rabbit IgG to VWF (Abcam, ab201336; 1:400), polyclonal rabbit IgG to MKI67 (Ki67; Thermo Scientific, PA5-16785; 1:500), and monoclonal mouse IgG1 to γ-H2AX (Millipore, 05-636; 1:200). Cells were washed four times with 1% BSA in DPBS–Tween 20 (DPBS-T), for 10 min each time, and then incubated for 1 h at RT in the dark with Alexa-Fluor-conjugated secondary antibodies (Life Technologies) (1:400, diluted in 2% BSA). Cells were washed again as described above, mounted with ProLong Diamond Antifade Mountant with DAPI (Life Technologies) onto Superfrost Plus (Thermo Scientific) slides, and imaged with an LSM510Meta confocal microscope (Zeiss).

Flow cytometry to assess cardiac-differentiation efficiency. For assessment of cardiac-differentiation efficiency, cells at day 15 of differentiation were dissociated with TrypLE Express for 5 min at 37 °C and transferred to flow cytometry tubes (BD Biosciences). Cells were then fixed with 4% PFA for 10 min, permeabilized with 0.1% saponin for 20 min, and stained using mouse monoclonal IgG1 to TNNT2 (conjugated to Alex Fluor 647) (13-11, BD Biosciences, 565744; 1:50) or mouse monoclonal IgG2b to MYH14 (conjugated to phycoerythrin) (MF20, BD Biosciences, 564408; 1:5) for 30 min at RT. Human skin fibroblasts showed no staining under these conditions (data not shown). Isotype controls—Alexa-Fluor-647-conjugated mouse IgG1 (BD Biosciences, 557714) and phycoerythrin-conjugated mouse IgG2b (BD Biosciences, 555743)—were used to establish gating. Cells were analyzed using a FACSAria II instrument (BD Biosciences) with a 100-μm nozzle and FACSDiva software. Data were analyzed using FlowJo X (TreeStar).

Cardiomyocyte plating and doxorubicin treatment. Cells at differentiation day 20 were dissociated using TrypLE Express that was freshly supplemented with liberase TH (50:1) for 15 min at 37 °C, centrifuged at 300*g* for 5 min, and filtered through a 100-μm cell strainer (Partec CellTrics). Live cells were counted, by staining with acridine orange and propidium iodide (AO/PI) and counting using a LUNA-FL Dual Fluorescence cell counter (Logos Biosystems), then plated onto Synthemax II–coated coverslip chamber sides (Nunc) in 24-well cell culture plates (750,000 live cells/well), 96-well black-sided plates (100,000 live cells/well, fluorescence) or 96-well white-sided plates (100,000 cells/well, luminescence) (all from Greiner), or in 24-well Seahorse plates (250,000 cells/well, Seahorse Bioscience), in CDM3 medium supplemented with 20% dialyzed FBS (Corning). Doxorubicin hydrochloride (HY-15142, MedChem Express) was resuspended to 10 mM in water for injection (WFI) (Corning). For cell treatments using day 30 hiPSC-CMs, cells were treated for 24 h to 96 h with doxorubicin (0.01–10 μM) diluted in CDM3M (without phenol red). For dexrazoxane treatment, hiPSC-CMs were treated with 100 mM dexrazoxane-HCl (HY-76201, MedChem Express) 12 h before doxorubicin administration, and then a second dose of 100 mM dexrazoxane was co-administered with doxorubicin. For *N*-acetyl-L-cysteine treatment, cells were co-treated with 1 mM *N*-acetyl-L-cysteine (A9165, Sigma-Aldrich) and doxorubicin.

Phase-contrast imaging and contraction assays. Phase-contrast images were captured using a Leica DMIR-LED microscope with a Leica DFC550 camera and Leica Application Suite 4.1 software. Contraction data were extracted using a Cellogy Pulse video microscope and an accompanying image-analysis platform[65].

Assays for plate-based cellular viability, caspase 3 and caspase 7, H_2O_2, GSH, and mitochondrial membrane potential. After doxorubicin treatment, PrestoBlue (Life Technologies) (10 μl) was added directly to each well of 96-well plates, followed by incubation at 37 °C for 2 h. Fluorescence was measured using a Cytation 5 Cell Imaging Multimode Reader (BioTek Instruments) with monochromators set to 560 nm (excitation) and 590 nm (emission). CCK-8 (Dojindo) (10 μl) was added directly to each well of the 96-well plates, followed by incubation at 37 °C for 4 h. Absorbance was then measured at 450 nm. CellTiter-Glo 2.0 (Promega) (100 μl) was added directly to each well of 96-well plates, followed by incubation at RT on an orbital shaker (Thermo) for 10 min. Fiber-optic luminescence was measured using a Cytation 5 Cell Imaging Multimode Reader (BioTek Instruments) with an integration time of 0.25 s. For all cell-viability assays, 10 μM staurosporine was used as a positive control. Assays using Caspase 3/7–Glo, ROS-Glo H_2O_2, and GSH-Glo (Promega) were performed following the manufacturer's instructions and read using fiber-optic luminescence using a Cytation 5 Cell Imaging Multimode Reader (BioTek Instruments) with an integration time of 1 s. Cell-viability assays using lactate dehydrogenase (LDH) (Clontech) and ToxiLight (an adenylate kinase–based assay) (Lonza) were performed following the manufacturers' instructions. For measurement of mitochondrial membrane potential, cells were stained at 37 °C for 30 min with JC-10 (Enzo Life Sciences) diluted to 2 μM in RPMI 1640, following which the cells were washed, and fluorescence was measured with monochromators set to 490 nm (excitation) and 520 nm (green) or 590 nm (red) (emission). 20 μM FCCP was used a positive control for the loss of mitochondrial membrane potential. Data were analyzed using Prism 6.0f software (GraphPad) using standard concentration–response guidelines.

Flow cytometry–based apoptosis, reactive oxygen species, mitochondrial membrane potential and DNA damage assays. After doxorubicin treatment, cells were dissociated with TrypLE Express and stained in suspension. For apoptosis detection, cells were stained with 7-AAD (7-aminoactinomycin D) and annexin V (both from BD Biosciences) following the manufacturer's instructions. 6 μM camptothecin (Sigma-Aldrich) was used as a positive control to set the flow cytometry gates. For DNA damage detection, cells were stained with anti–phospho-histone γ-H2AX (Millipore) and propidium iodide (Life Technologies) following standard protocols[66]. For whole-cell reactive oxygen species detection, cells were incubated with 1 μM CellROX Green (Life Technologies) for 30 min; dead cells were excluded using SYTOX Red (Life Technologies). 20 μM menadione (Sigma-Aldrich) was used as a positive control to induce the production of reactive oxygen species. For mitochon-

© 2016 Nature America, Inc. All rights reserved.

doi:10.1038/nm.4087

drial superoxide detection, cells were incubated with 5 µM MitoSOX Red (Life Technologies) for 30 min; dead cells were excluded using SYTOX Green (Life Technologies). 20 µM antimycin A (Sigma-Aldrich) was used as a positive control for the production of mitochondrial superoxides[67]. Cells were analyzed by flow cytometry on a BD Biosciences FACS Aria II instrument using FACSDiva software. Data analysis was performed using FlowJo X (TreeStar).

RNA-seq gene expression analysis. hiPSC-CMs were treated with doxorubicin for 24 h. Cells were dissociated with TrypLE Express and Liberase TH and centrifuged. Cell pellets were flash-frozen in liquid nitrogen and stored at −80 °C. RNA was extracted using a micro RNeasy kit (QIAGEN) and cDNA synthesis, library preparation and sequencing on a HiSeq 2000 instrument (Illumina) was performed by Macrogen. 40 million reads (20 million in each direction) was used for each sample.

Microarray data analysis. hiPSC-CMs were treated with doxorubicin for 24 h. Cells were dissociated with TrypLE Express and Liberase TH and centrifuged. Cell pellets were flash-frozen in liquid nitrogen and stored at −80 °C. RNA was extracted using a micro RNeasy kit (QIAGEN). Samples were processed by the Stanford Functional Genomics Facility using Affymetrix chips and Agilent Scanner. The probe-level data was preprocessed with the Robust Multiarray Analysis (RMA) algorithm[68], quantile normalized[69], and summarized to the gene level.

RNA-seq data analysis and coding sequence variant calling. RNA-seq analysis was performed on hiPSC-CMs from six patients (three DOX and three DOXTOX samples), each treated with 0 µM or 1 µM doxorubicin. Reads were mapped to the hg19 reference human genome using tophat2 software (version v2.0.13)[70], assembled into transcripts using cufflinks (version 2.2.1) and cuffmerge with known transcripts as guides[71], and quantified using cuffdiff (version 2.2.1). Only transcripts mapped to unique genes were retained. The read-counts of transcripts were aggregated to the gene level by summation. Gene expression was then $\log_2$-transformed with a pseudocount of 1, and quantile-normalized[69]. Only known protein-coding genes were retained for subsequent analysis. Gene variant-calling from the RNA-seq data was performed using samtools (version 1.2) and bcftools (version 1.2)[72] and annotated with the Genome Analysis Toolkit (version v3.4–46)[14]. The mutation effects of the variants were predicted using snpEff[73]. The variant-calling results were visualized and inspected using the integrative genome viewer[74].

Independent component analysis (ICA). ICA is an unsupervised machine-learning method for solving the blind-source separation problem[75]. Given a $g \times s$ matrix X for the log-transformed expression values of g genes in s samples, ICA estimates a $g \times m$ source matrix S for m independent gene modules, and an $m \times s$ matrix A of mixing coefficients of the m modules in the s samples, such that $X \approx S \times A$. ICA has been shown to identify a higher number of functionally coherent gene clusters than previous methods such as K-means clustering or principle component analysis[39,76]. We applied ICA to derive statistically independent gene modules (pathways) in the doxorubicin drug-treatment data. GO-enrichment analysis was performed using Fisher's exact test algorithm[77]. To compare the patient-response study (RNA-seq analysis of DOX versus DOXTOX) and the concentration–response study (microarray analysis of 0–10 µM doxorubicin), we projected patient-response data Y onto the ICA modules S derived from the concentration–response data X to obtain the estimated expression of these modules (i.e., $A_Y = S^t \cdot Y$, where S^t is the transpose of S).

Inference of transcription factor activity in gene expression data. To infer the involvement of transcription factors in a biological process, we applied Fisher's exact test to evaluate if the target genes of each transcription factor are significantly over-represented in the up- and downregulated gene sets in the microarray data. We defined upregulated, downregulated, and unchanged genes for each of m gene modules as those with s.d.-normalized expression values of $z \geq q_{0.95}$, $z \leq q_{0.95}$, and $-q < z < q_{0.95}$, respectively, where $q_{0.95}$ is the 95% quantile of standard normal distribution. The transcription factor target gene database was compiled from literature-reported regulatory relationships using low-throughput experiments, as well as from ENCODE[78] and from additional chromatin immunoprecipitation (ChIP)-seq data sets retrieved from Gene Expression Omnibus[79]. Two-tailed Fisher's exact tests were performed. For transcriptional regulatory network visualization, we used a linear model per gene module to estimate the activity values of each transcription factor in our transcription factor target gene database. The P values of transcription factor activities were obtained from the Wald test of the estimated activities, and q values were then estimated from the P values.

Estimation of gene expression changes associated with patient-specific doxorubicin toxicity responses. Body mass index (BMI) is known to affect doxorubicin dosing and responses. To reduce the effect from BMI, we required the BMI of the selected patients to be in the range of 25 to 34. In addition, we included BMI as a control variable in the linear model when estimating patient-specific doxorubicin responses. Specifically, to extract the differential response between DOX and DOXTOX patients upon doxorubicin treatment, the following linear model was applied to each gene, for observed gene expression level x_{id} for patient i (1–6) and doxorubicin concentrations d(0 µM, 1 µM):

$$x_{id} \sim \mu + b_i \cdot (\beta_b + d \cdot \beta_{bd}) + t_i \cdot (\beta_t + d \cdot \beta_{td}) + \beta_d + \varepsilon_{id},$$

where b_i and t_i are the BMI and response type (DOX or DOXTOX), respectively. β_b, β_t, and β_d are the effects of BMI, patient type, and doxorubicin treatment on gene expression. β_{bd} and β_{td} are the interaction effects of BMI and doxorubicin treatment, and patient-response type and doxorubicin treatment, respectively. We did not strictly control for age in patient selection, and there was a spurious inverse correlation between patient age and toxicity response in our data set ($R = -0.81$, $P = 0.052$). Because we found that including age as a control variable did not change the major findings, we present the results based on the model that does not include age as a variable. In addition, age is not a known risk factor for doxorubicin cardiotoxicity. Despite these considerations, it is possible that the identified patient-specific drug responses and regulatory mechanisms could be partly due to uncontrolled age differences between the patients.

Seahorse extracellular metabolic-flux assay. hiPSC-CMs were plated at 250,000 cells per well in Synthemax II–coated Seahorse 24-well plates in CDM3M. The bioenergetics responses of hiPSC-CMs were measured with the Seahorse Bioscience XF24 Flux Analyzer following directions in the XF Cell Mito Stress Test Kit User Guide. Medium was aspirated and replaced with 525 µl assay medium (Seahorse Bioscience) and pre-equilibrated for 1 h at 37 °C. Baseline OCR measurements were performed, followed by injection of 1 µM oligomycin and three OCR measurements, followed by injection of 0.5 µM FCCP and three OCR measurements, and finally followed by injection of 0.5 µM rotenone and 0.5 µM antimycin A and three OCR measurements. Four hiPSC lines were used for each sample group and three technical replicates were performed. To confirm plating homogeneity, the 0-µM well from each set of samples was stained with NucBlu Live Ready Probes reagent, and the number of cells in the well was counted with a high-content imager (Biotek Cytation 5).

Mitochondrial copy-number quantification. Cells were dissociated with TrypLE Express, and the pellets were flash-frozen in liquid nitrogen. Genomic DNA (gDNA) extraction was performed using DNeasy Blood and Tissue Kit (QIAGEN), according to the manufacturer's instructions, with RNase treatment. Following determination of gDNA concentration using a UV-vis spectrophotometer, all samples were adjusted to have equal gDNA concentrations. The mitochondrial DNA (mtDNA) content of cells is expressed as a relative mtDNA:nuclear DNA (nDNA) ratio; the nDNA copy number per cell is considered to be constant, such that alteration of the ratio is attributed to changes in mtDNA content. Real-time PCR amplification for a nuclear gene, *SDHA* (encoding succinate dehydrogenase complex, subunit A, flavoprotein variant), and a mitochondrial gene, *ND1* (encoding NADH dehydrogenase subunit I), was performed using an ABI Prism 7000 Sequence Detection System.

© 2016 Nature America, Inc. All rights reserved.

Total oxidative phosphorylation protein analysis. Immunoblotting was performed using standard BioRad wet-blot protocols and Total OXPHOS Antibody Cocktail (Abcam, ab110413), containing an optimized premixed cocktail of 5 monoclonal antibodies (mAbs), one each against: complex I subunit NDUFB8 (20 kDa; a subunit of NADH dehydrogenase; ab110242), complex II subunit SDHB (30 kDa: a subunit of succinate dehydrogenase; ab14714), complex III subunit UQCRC2 (48 kDa; a component of the ubiquinol–cytochrome *c* reductase complex; ab14745), complex IV subunit MTCO1 (40 kDa; a subunit of cytochrome *c* oxidase; ab14705), and complex V ATP5A (55 kDa; a subunit of ATP synthase; ab14748). α-tubulin (ab7291) was used as a loading control.

Calcium imaging. Dissociated hiPSC-CMs were reseeded in Matrigel-coated 8-well Lab-Tek II coverglass chambers (Thermo Scientific Nunc) and treated with 5 μM Fluo–4 a.m. (Life Technologies) and 0.02% Pluronic F-127 (Life Technologies) in Tyrode's solution (140 mM NaCl, 5.4 mM KCl, 1 mM MgC l_2, 10 mM glucose, 1.8 mM $CaCl_2$, 10 mM HEPES, pH 7.4 with NaOH for 15 min at 37 °C). Cells were then washed with Tyrode's solution, and Ca^{2+} imaging was conducted using a Zeiss LSM 510Meta confocal microscope (Carl Zeiss AG) with a 63× objective and analyzed using Zen imaging software. Measurements of spontaneous Ca^{2+} transients were obtained at 37 °C using a single-cell line-scan mode.

Statistical methods. Data were analyzed in Excel or R and graphed in Prism (GraphPad). Data are presented as mean ± s.e.m. Comparisons were conducted via Fisher's exact test, one-way ANOVA test followed by all-pairwise-multiple-comparison procedures (Holm–Sidak method), or via an unpaired, two-tailed Student's *t*-test with significant differences defined by $P < 0.05$ (*), $P < 0.01$ (**), and $P < 0.001$ (***). No blinding or randomization was used. Our sample size (four patients in each category) was based on the feasibility of handling of 12 hiPSC lines. Patient exclusion criteria are outlined in **Supplementary Table 1**.

60. Melkoumian, Z. *et al.* Synthetic peptide-acrylate surfaces for long-term self-renewal and cardiomyocyte differentiation of human embryonic stem cells. *Nat. Biotechnol.* **28**, 606–610 (2010).
61. Chen, G. *et al.* Chemically defined conditions for human iPSC derivation and culture. *Nat. Methods* **8**, 424–429 (2011).
62. Fusaki, N., Ban, H., Nishiyama, A., Saeki, K. & Hasegawa, M. Efficient induction of transgene-free human pluripotent stem cells using a vector based on Sendai virus, an RNA virus that does not integrate into the host genome. *Proc. Jpn. Acad., Ser. B, Phys. Biol. Sci.* **85**, 348–362 (2009).
63. Mali, P. *et al.* Butyrate greatly enhances derivation of human induced pluripotent stem cells by promoting epigenetic remodeling and the expression of pluripotency-associated genes. *Stem Cells* **28**, 713–720 (2010).
64. Thomson, J.A. *et al.* Embryonic stem cell lines derived from human blastocysts. *Science* **282**, 1145–1147 (1998).
65. Maddah, M. *et al.* A non-invasive platform for functional characterization of stem cell–derived cardiomyocytes with applications in cardiotoxicity testing. *Stem Cell Rep.* **4**, 621–631 (2015).
66. Huang, X. & Darzynkiewicz, Z. Cytometric assessment of histone H2AX phosphorylation: a reporter of DNA damage. *Methods Mol. Biol.* **314**, 73–80 (2006).
67. Mukhopadhyay, P. *et al.* Simultaneous detection of apoptosis and mitochondrial superoxide production in live cells by flow cytometry and confocal microscopy. *Nat. Protoc.* **2**, 2295–2301 (2007).
68. Irizarry, R.A. *et al.* Exploration, normalization, and summaries of high-density oligonucleotide array probe level data. *Biostatistics* **4**, 249–264 (2003).
69. Bolstad, B.M., Irizarry, R.A., Astrand, M. & Speed, T.P. A comparison of normalization methods for high-density oligonucleotide array data based on variance and bias. *Bioinformatics* **19**, 185–193 (2003).
70. Kim, D. *et al.* TopHat2: accurate alignment of transcriptomes in the presence of insertions, deletions, and gene fusions. *Genome Biol.* **14**, R36 (2013).
71. Trapnell, C. *et al.* Differential gene and transcript expression analysis of RNA-seq experiments with TopHat and Cufflinks. *Nat. Protoc.* **7**, 562–578 (2012).
72. Li, H. *et al.* The sequence alignment–map format and SAMtools. *Bioinformatics* **25**, 2078–2079 (2009).
73. Cingolani, P. *et al.* A program for annotating and predicting the effects of single-nucleotide polymorphisms, SnpEff: SNPs in the genome of *Drosophila melanogaster* strain w^{1118};*iso-2*;*iso-3*. *Fly (Austin)* **6**, 80–92 (2012).
74. Robinson, J.T. *et al.* Integrative genomics viewer. *Nat. Biotechnol.* **29**, 24–26 (2011).
75. Hyvärinen, A. & Oja, E. Independent component analysis: algorithms and applications. *Neural Netw.* **13**, 411–430 (2000).
76. Lee, S.-I. & Batzoglou, S. Application of independent component analysis to microarrays. *Genome Biol.* **4**, R76 (2003).
77. Alexa, A., Rahnenführer, J. & Lengauer, T. Improved scoring of functional groups from gene expression data by de-correlating GO graph structure. *Bioinformatics* **22**, 1600–1607 (2006).
78. Gerstein, M.B. *et al.* Architecture of the human regulatory network derived from ENCODE data. *Nature* **489**, 91–100 (2012).
79. Barrett, T. *et al.* NCBI GEO: archive for functional genomics data sets—update. *Nucleic Acids Res.* **41**, D991–D995 (2013).

© 2016 Nature America, Inc. All rights reserved.